Hydrogenic Lamb shift in Ge^{31+} and the fine-structure Lamb shift

C. T. Chantler*
School of Physics, University of Melbourne, Victoria 3010, Australia

J. M. Laming
Space Science Division, Code 7674L, Naval Research Laboratory, Washington, DC 20375, USA

J. D. Silver
Clarendon Laboratory, University of Oxford, Parks Road, Oxford OX1 3PU, United Kingdom

D. D. Dietrich
Lawrence Livermore National Laboratory, Livermore, California 94550, USA

P. H. Mokler
Max-Planck-Institut fur Kernphysik, D-69117 Heidelberg, Germany
and Gesellshaft für Schwerionenforschung (GSI), D-6100 Darmstadt, Germany

E. C. Finch
Department of Pure and Applied Physics, Trinity College, Dublin, Ireland

S. D. Rosner
University of Western Ontario, London, Ontario, Canada N6H 3K7
(Received 30 March 2009; published 14 August 2009)

Using x-ray diffraction and beam-foil spectroscopy, we have determined precise wavelengths for Lyman α_1 and Lyman α_2 in hydrogenic germanium of $1.166\,993\,8 \pm 33 \pm 169$ and $1.172\,433\,6 \pm 39 \pm 170$ Å. Hydrogenic germanium Ge^{31+} $1s$-$2p_{3/2}$ and $1s$-$2p_{1/2}$ Lamb shifts are measured to be $66\,080 \pm 237 \pm 1121$ and $67\,169 \pm 281 \pm 1237$ cm^{-1}, respectively. This 14 ppm measurement of the wavelengths thus provides a 1.8% measurement of the $2p$-$1s$ Lamb shift and is an improvement by a factor of 3 over previous work. Fitting the full two-dimensional dispersion relation, including Balmer and Lyman series, limits random and systematic correlation of parameters. Dominant systematics are due to diffraction parameters including crystal thickness and alignment, differential Doppler shifts due to the variable location of spectral emission downstream of the beam-foil target, and dielectronic, $2s$-$1s$, and $4f$-$2p$ satellites. Models developed are applicable to all relativistic plasma modeling in beam-foil spectroscopy at accelerators. The technique also reports the germanium $2p_{3/2}$-$2p_{1/2}$ fine structure as $397\,617 \pm 251 \pm 512$ cm^{-1}, representing a 0.14% measurement of the fine structure and a 71% measurement of the QED contribution to the hydrogenic germanium fine structure, an improvement of a factor of 6 over previous work. We also report a precise measurement of heliumlike resonances and fine structure.

DOI: 10.1103/PhysRevA.80.022508 PACS number(s): 31.30.jf, 12.20.Fv, 34.80.Dp, 32.30.Rj

I. INTRODUCTION AND OVERVIEW

The use of beam-foil spectroscopy for the production of highly charged ions is well known [1–3]. In particular, the production of one- and two-electron species by this method permits a precise test of QED [4–8]. Theoretical evaluation of the hydrogenic and heliumlike energy levels enables derivation of the Lamb shifts.

Impressive precision of low-Z measurements has led to investigations of nuclear form factors and polarization, which involve interesting physics in their own right [8,9]. Meanwhile, medium-Z techniques have been developed over the last two decades, with a view to probing QED in the regime of high effective coupling strength [10–12]. Motivation arises from the increasing significance of higher-order QED terms, together with the $(Z\alpha)^4$ dependence of the lowest order QED contributions, depending on the formalism used for the theoretical expansions [13,14]. The dependence upon $Z\alpha$ indicates another strong motivation for these investigations, namely, that as $Z\alpha$ approaches unity for high-Z elements, the convergence of higher-order terms may fail, and additional interactions may in principle be observed.

However, rate processes and relative intensities inside and outside the foil have not received the same attention. With sufficient precision, these may be used to deduce dominant interactions within the foil. This corresponds to a dominant uncertainty in beam-foil measurements because of differential source and cascade locations and hence differential Doppler shifts, as we discuss. The effect on absolute and relative x-ray emission intensities as a function of target thickness is compared to model predictions. The observation of one- and two-electron spectra as a function of foil thickness allows

*chantler@unimelb.edu.au

estimation of the relative cross sections for excitation to different states.

This paper is a sequel to an earlier presentation [6,15] of part of this experimental data but presents analysis and additional data to resolve particular issues and assess the significance of systematics and satellites in greater detail. The basic analytic approach has been discussed in two recent papers [16,17] so that a series of references will be made to that logic, allowing this paper to be efficiently presented.

Nonetheless, we will introduce the Lyman-α–Balmer-β intercomparison technique (Sec. II) and the experimental setup (Sec. III) especially where it deviates from [16,17]. We then discuss key logical steps in subsequent experimental sections on photographic detection (Sec. IV) and solid state detectors (Sec. V).

Theoretical wavelengths are discussed in Sec. VI, together with the basic equations of analysis of the experimental data (Sec. VII). This paper briefly summarizes fitting procedures to explain the technique "beyond the Lyman α–Balmer β intercomparison" in Sec. VIII. Relative intensities from the Si(Li) detectors are presented in Sec. IX and observations are given in Sec. X. We consider the effect of Doppler angles on the spectra (Sec. XI) and are then able to introduce the photographic data and key additional effects due to crystal perfection and polarization in Sec. XII, investigating crystal mosaicity and refractive index depth penetration systematic corrections. We present the scales between the (abstract) diffraction theory and the explicit measured positions in microns around the film. We are then in a position to incorporate the data from both the Si(Li) detectors and the crystal diffraction (Sec. XIII). Satellite intensities and contributions are discussed in Sec. XIV.

Cascade contributions are modeled in Sec. XV beginning with the quantification of observed normalised ratios, discussion of polarization dependencies, heliumlike transitions, and traditional dielectronic species; but then leading to new discussion of Lyman γ $3l$-$1s$, Lyman $2s$-$1s$, and Balmer $4f$-$2p$ contributions, a significant uncertainty in past modeling. This gives a detailed discussion of theoretical models. Armed with this, we tabulate model predictions compared to experimental data. A separate section (Sec. XVI) discusses satellite locations. Systematics relating to satellite contamination, crystal and diffraction effects, and Doppler shifts relating to differences in decay location of specific states of interest lead to tabulated results in Sec. XVII. Fitting the full two-dimensional dispersion relation, including other members of Balmer and Lyman series, significantly limits correlation of parameters, revealing major systematics due to dynamical diffraction depth penetration and to the decay location. The fine-structure separation is determined to high accuracy, and the fine-structure QED contributions are compared with theory in Sec. XVIII.

We have measured secondary wavelengths of satellite heliumlike transitions which could have affected the primary measurements of Lyman-α and Balmer-β components and present these in Sec. XIX. Finally we summarize the conclusions of this paper (Sec. XX).

TABLE I. Summary of germanium data collected.

Run	Z	Exposures $E(f)$ SS1,Si(Li) (mC)	Target (μg cm^{-2}, C)	Stripper
20[a,b]	32	0.708,0.708	25	400
21[a]	32	4.05,4.05	50	400
22[a]	32	9.501,10.211	50	680
23[a]	32	4.00,4.00	238	680
24[c]	32	4.00,4.00	238	680
25[a]	32	18.0,12.7	10	680
26[c]	32	13.77,14.00	10	680
27[a,c]	32	8.00,7.45	50	680
28[a,c]	32	9.10,8.99	25	680

[a]New foil.
[b]Fogging check (weak spectrum).
[c]Calibrated by X-ray source after run.

II. LYMAN α–BALMER β ALIGNMENT AND SPECTROMETRY

Lyman α radiation is nearly exactly four times the energy of Balmer-β radiation, with deviation following mainly from relativistic and QED corrections to the Bohr model. Diffraction of Lyman-α radiation in fourth order with appropriate crystals will provide an in-beam calibration source with the same ions (and ion velocities) so that the Doppler shift is identical for all lines. This then provides a precise $n=2-1$ versus $n=4-2$ Lamb shift measurement [5]. This comparison involves a quite different principle from the use of multiple references to many-electron in-beam calibration lines [18].

The strong $2p$-$4d$ components lie on either side of the $1s$-$2p$ transitions, and crystal resolution in the $Z=22-40$ region is adequate to fully resolve the $2p_{3/2}$-$1s$ and $2p_{1/2}$-$1s$ Lyman $\alpha_{1,2}$ transitions. Diffracting efficiencies for both first- and fourth-order lines yield good statistics in a reasonable period of accelerator beam time. Targets are mounted in a collimating target holder with the (carbon) foil upstream to avoid occlusion of x-rays from the rear surface.

III. EXPERIMENTAL

Following a procedure similar to that of the Lyman α measurement in Fe^{25+} at Lawrence Berkeley Laboratory [5], a beam of bare nucleii was allowed to capture an electron from a carbon target at GSI. The 15 MeV/amu Ge ions were foil stripped by either 400 or 680 μg/cm^2 carbon foils after the last accelerator cavity. The fully stripped ions were then selected by a bending magnet for the experiment. Typical currents of naked Ge ions delivered to the experiment were 500 nA (680 μg/cm^2 foil) and 90–150 nA (400 μg/cm^2 foil). The thicknesses of the carbon target foils used were 10, 25, 50, and 238 μg/cm^2. Beam divergence was minimized by observation of profile monitors upstream and downstream of the target. Conditions are summarized in Table I.

This "pickup" method yields very low satellite and heliumlike contamination of the spectra, as discussed below. The

TABLE II. Estimated attenuation corrections and parameters for Si(Li) detectors A and B. A: 17° to the beam; B: 90° to the beam; and $\bar{t}$: estimated mean dead layer.

Transition	Energy (keV)	Mylar 5 μm A, B	Air gap 10 ± 1 mm A, B	Au contact 0.021 μm A, B	Be(B) 12 μm B	Be(A) 3 μm A	$\bar{t}$ 0.5 μm	Efficiency $(\bar{t}_B)$[a] 90° Si(Li) B	Efficiency $(\bar{t}_A)$[b] 17° Si(Li) A	Uncertainty dead layer+air gap
Balmer α	1.973	0.824	$0.509\pm7.0\%$	0.972	0.848	0.960	0.717	4.18×10^{-7}	4.98×10^{-7}	$\pm13.5\%$
Balmer β	2.662	0.922	$0.753\pm2.9\%$	0.945	0.939	0.984	0.855	8.38×10^{-7}	1.038×10^{-6}	$\pm6.0\%$
Balmer γ	2.980	0.943	$0.815\pm2.1\%$	0.951	0.957	0.989	0.891	9.78×10^{-7}	1.225×10^{-6}	$\pm4.3\%$
Balmer δ	3.153	0.952	$0.859\pm1.5\%$	0.956	0.964	0.991	0.905	1.065×10^{-6}	1.353×10^{-6}	$\pm3.6\%$
Lyman spectra		0.999	$0.997\pm0.1\%$	0.998	1.000	1.000	0.997	1.496×10^{-6}	1.962×10^{-6}	$\pm0.1\%$

[a] $\bar{t}_B=0.336$ μm: estimated dead layer B.
[b] $\bar{t}_A=0.664$ μm: estimated dead layer A.

experiment had four primary detectors. The dual-arm Johann x-ray crystal spectrometer SS1 developed at Lawrence Livermore National Laboratory [19–21] is the main tool for high-accuracy measurement of transition energies and Lamb shifts and has two separate crystals mounted to check and account for Doppler shifts or crystal defects.

In this experiment, the spectrometer was supported by observations at 17° to the beam with a lithium-drifted silicon detector and observations at 90° with a similar detector (see Sec. V for solid angles). These are particularly useful for investigating the Balmer and Lyman series, possible satellites or contamination, and hence the plasma processes for excitation (see Sec. XIV).

The dual-arm spectrometer used a Si 111 dispersing crystal curved to $2R=300$ mm in the Johann mounting, with photographic detection using Kodak DEF 392 x-ray film. The relative intensities from the dual-arm spectrometer resolved Balmer components to the lines and provide information regarding statistical and non-statistical redistribution processes. The dual-arm Johann spectrometer measured the $1S_{1/2}$-$2P_{1/2,3/2}$ Lyman α transitions in fourth order from a diffracting crystal simultaneously with the $n=2-n=4$ Balmer β transitions in first order. Also observable are Lyman β and Balmer δ transitions, together with Balmer γ and Balmer ϵ, and Lyman γ, and heliumlike resonances.

Silicon 111 crystals were used for the high energy x rays from $Z=32$ and are structurally robust and reliable. Spectrometer alignment and calibration details are given in [6]. Crystals were formed to a cylindrical curvature. This remains common practice for many experiments especially including two-dimensional curvatures, but more uniform cylindrical curvature arises from a variety of bending methods [22,23]. Nonetheless, this curvature method was found to give generally good focusing. More recent developments are discussed elsewhere [24], especially including high-accuracy curvature methods for triangular crystals [12]. Crystals are left in their individual mounts for the duration of the experiment and no drift of curvature with time is observed.

IV. PHOTOGRAPHIC DETECTION

The dual-arm Johann spectrometer with formed crystal bending uses photographic detection with Kodak DEF-392 x-ray emulsion. The Kodak DEF-392 film window covers Bragg angles from 27.6° to 72°, reduced by the spectrometer baffle and crystal range to approximately 35°–53° for uniform source intensity (the whole source being imaged by the crystal). This detection method, like the use of image plates, simultaneously observes the whole spectrum, focused, thus eliminating errors from beam fluctuations in energy, location, angle, and intensity (to first and second order) and reducing collection times per experiment. Photographic exposures were labeled 20–28, with a suffix U or L for the upper and lower Rowland circles.

Theory and modeling have been developed to interpret the experimental photographic data [22,25–27]. Linearized relative intensities are derived with absolute accuracy given by the pseudobinomial grain statistic so that spectra of $(I\pm\delta I)$ along two dimensions may then be used as inputs for later analysis [16].

The first method for digitization and linearization of these data is mentioned elsewhere [6], and the general method has also been discussed [16]. The work reported here uses new densitometry, calibrated axes, and functional dependence for an area map of densitized strips, an accurate linearization procedure, and then derives parameters and particularly relative intensities from the sets of scans for each film using weighted fits and propagated error analysis. In this respect the analysis of all spectral components is made on a robust and uniform basis with well-defined error bars, and conclusions are more robust.

V. SOLID-STATE DETECTION

The bulk of the Si(Li) data was gained using the Si(Li) detector mounted at 17° to the beam. The Si(Li) detector at 90° to the beam provided data when the intervening crystal mount of the dual-arm device was removed for testing and calibration purposes. It provides confirmation of the intensities, efficiency corrections, and isotropy, but not a main data set.

Relative efficiency corrections from Si(Li) detector arrangements are given in Table II. The Si(Li) detector mounted at 17° to the beam had a 10 mm^2 active area at 530 mm from the beam through a 10 mm air gap, a 5 μm Mylar window, and an attenuator. The detector normal to the

beam had an active area of 80 mm^2 at 649 mm from the source through a 10 mm air gap, a 5 μm Mylar window, and a 10% transmission copper grid. The beryllium detector windows were 3 and 12 μm, respectively, and the gold contact layers and silicon dead layers of the detectors were estimated as 0.021 and 0.5 μm, respectively.

The attenuators were fine copper meshes with no transmission (at our energies) for observed radiation. Detector A had a solid angle of $\frac{\Omega}{4\pi}=2.833\times10^{-6}$, with a 0.70($\pm$0.04) attenuator. Detector B had a solid angle of $\frac{\Omega}{4\pi}=1.511\times10^{-5}$, with a 10% attenuator. These factors are included in the total estimated efficiencies.

Rough calibration of the Si(Li) detectors, alignment detectors (a proportional counter and a HgI_2 detector) and the SS1 used an x-ray source with a mixed Ga, S, Ni, and Cu anode located approximately at the target foil position. *K* and *L* x-rays were excited by 20 keV electron bombardment. Ag lines are observed from silver epoxy used to form the conducting anode. This calibration was put on half of the photographic spectra to allow direct comparison. They have a complex structure but are adequate for Si(Li) calibration. Am^{241} and Co^{57} sources were also used prior to the experiment to calibrate the Si(Li) detectors.

Preliminary exposures allowed comparison of the two Si(Li) detectors; The 90° detector observed anode calibration spectra and heliumlike satellite contamination from downstream metastables but was occluded by the film holder in the main scans. The 17° detector observed the target throughout data collection but was partially occluded by the calibration anode support and did not observe (far) downstream decays. Detector resolution (175–185 eV for Mn $K\alpha$) and linearity were adequate to identify observed peaks but not of course to resolve Lyman α components. Their primary purpose was to observe relative intensities, measure satellite, and heliumlike contamination and to allow optimization of the Lyman-Balmer ratio.

A discrepancy between (raw) Balmer-α intensity ratios in the detectors of 26% is consistent with the different estimated dead layers within the corresponding uncertainty. Note that this uncertainty is quite small, reduces to $<1\%$ for the Lyman series, and the relative values are confirmed by the photographic analysis.

VI. THEORETICAL INPUT

The two most comprehensive theoretical approaches [28,29] agree for $n=1$ and $n=2$ levels. For the higher-*n* levels and Balmer transition energies, values of Erickson [30] must be corrected for improved values of constants, Dirac energies, and QED terms [22] (particularly Bethe logarithms [31]). Estimated theoretical uncertainties lie at the few ppm of transition wavelengths. Heliumlike resonance transition wavelengths follow Drake [32] and Vainshtein [33,46], with corrections of the latter for higher-*n* levels [22]. Because of these corrections, a detailed summary of relevant theoretical transition energies is given in Table III.

VII. BRAGG DIFFRACTION, DOPPLER SHIFTS, AND ANALYTIC DEVELOPMENT

The double-crystal setup (SS1) provides information on Doppler shifts from comparison of the spectra from each

TABLE III. Theoretical wavelengths and uncertainties used for important components (no Doppler or refractive index shifts included in this table). On good plates most of these peaks were identifiable with some of the fine structure unresolved. (a) Diffraction in third to fifth order. (b) Diffraction in first order, also showing the location of higher-order Lyman spectra.

$^{32}Ge^{74}$ λ	Identification
	(a)
0.8962136 ± 20 Å	Lyman ζ $1s_{1/2}$-$7p_{3/2}$
0.8962876 ± 4 Å	Lyman ζ $1s_{1/2}$-$7p_{1/2}$
0.9029443 ± 20 Å	Lyman ε $1s_{1/2}$-$6p_{3/2}$
0.9030640 ± 4 Å	Lyman ε $1s_{1/2}$-$6p_{1/2}$
0.9143372 ± 4 Å	Lyman δ $1s_{1/2}$-$5p_{3/2}$
0.9145495 ± 4 Å	Lyman δ $1s_{1/2}$-$5p_{1/2}$
0.9360870 ± 4 Å	Lyman γ $1s_{1/2}$-$4p_{3/2}$
0.9365222 ± 4 Å	Lyman γ $1s_{1/2}$-$4p_{1/2}$
0.9867935 ± 5 Å	Lyman β $1s_{1/2}$-$3p_{3/2}$
0.9879423 ± 6 Å	Lyman β $1s_{1/2}$-$3p_{1/2}$
1.0247816 ± 19 Å	$1s2\ ^1S_0$-$1s3p\ ^1P_1$
1.0252736 ± 19 Å	$1s2\ ^1S_0$-$1s3p\ ^3P_2$
1.0262384 ± 19 Å	$1s2\ ^1S_0$-$1s3p\ ^3P_1$
1.0263022 ± 19 Å	$1s2\ ^1S_0$-$1s3p\ ^3P_0$
1.1669630 ± 7 Å	Lyman α $1s_{1/2}$-$2p_{3/2}$
1.1723988 ± 7 Å	Lyman α $1s_{1/2}$-$2p_{1/2}$
1.2060561 ± 26 Å	$1s2\ ^1S_0$-$1s2p\ ^1P_1$
1.2085660 ± 26 Å	$1s2\ ^1S_0$-$1s2p\ ^3P_2$
1.2130664 ± 26 Å	$1s2\ ^1S_0$-$1s2p\ ^3P_1$
1.2133829 ± 26 Å	$1s2\ ^1S_0$-$1s2p\ ^3P_0$
nλ	
	(b)
3.6416102 ± 120 Å	Balmer 8 $2p_{1/2}$-$10d_{3/2}$
3.6573489 ± 16 Å	Lyman δ $1s_{1/2}$-$5p_{3/2}$ (forth order)
3.6581982 ± 16 Å	Lyman δ $1s_{1/2}$-$5p_{1/2}$ (forth order)
3.6771654 ± 120 Å	Balmer 7 $2p_{1/2}$-$9d_{3/2}$
3.6777364 ± 113 Å	Balmer 7 $2p_{1/2}$-$9s_{1/2}$
3.6784217 ± 120 Å	Balmer 7 $2s_{1/2}$-$9p_{3/2}$
3.6790079 ± 113 Å	Balmer 7 $2s_{1/2}$-$9p_{1/2}$
3.6950720 ± 120 Å	Balmer 8 $2p_{3/2}$-$10d_{5/2}$
3.7278667 ± 120 Å	Balmer ζ $2p_{1/2}$-$8d_{3/2}$
3.7287029 ± 113 Å	Balmer ζ $2p_{1/2}$-$8s_{1/2}$
3.7291579 ± 120 Å	Balmer ζ $2s_{1/2}$-$8p_{3/2}$
3.7300162 ± 113 Å	Balmer ζ $2s_{1/2}$-$8p_{1/2}$

TABLE III. (*Continued.*)

$^{32}Ge^{74}$ nλ	Identification
	(b)
3.7314870 ± 120 Å	Balmer 7 $2p_{3/2}$-$9d_{5/2}$
3.7316841 ± 120 Å	Balmer 7 $2p_{3/2}$-$9d_{3/2}$
3.7322722 ± 113 Å	Balmer 7 $2p_{3/2}$-$9s_{1/2}$
3.7443478 ± 16 Å	Lyman γ $1s_{1/2}$-$4p_{3/2}$ (forth order)
3.7460890 ± 16 Å	Lyman γ $1s_{1/2}$-$4p_{1/2}$ (fourth order)
3.7836221 ± 120 Å	Balmer ζ $2p_{3/2}$-$8d_{5/2}$
3.7839106 ± 120 Å	Balmer ζ $2p_{3/2}$-$8d_{3/2}$
3.7847721 ± 113 Å	Balmer ζ $2p_{3/2}$-$8s_{1/2}$
3.8044024 ± 125 Å	Balmer ε $2p_{1/2}$-$7d_{3/2}$
3.8057033 ± 117 Å	Balmer ε $2p_{1/2}$-$7s_{1/2}$
3.8057472 ± 125 Å	Balmer ε $2s_{1/2}$-$7p_{3/2}$
3.8070828 ± 117 Å	Balmer ε $2s_{1/2}$-$7p_{1/2}$
3.8623404 ± 125 Å	Balmer ε $2p_{3/2}$-$7d_{5/2}$
3.8627892 ± 125 Å	Balmer ε $2p_{3/2}$-$7d_{3/2}$
3.8641304 ± 117 Å	Balmer ε $2p_{3/2}$-$7s_{1/2}$
3.9287193 ± 138 Å	Balmer δ $2p_{1/2}$-$6d_{3/2}$
3.9301534 ± 138 Å	Balmer δ $2s_{1/2}$-$6p_{3/2}$
3.9309282 ± 129 Å	Balmer δ $2p_{1/2}$-$6s_{1/2}$
3.9324210 ± 129 Å	Balmer δ $2s_{1/2}$-$6p_{1/2}$
3.9471742 ± 20 Å	Lyman β $1s_{1/2}$-$3p_{3/2}$ (fourth order)
3.9517691 ± 24 Å	Lyman β $1s_{1/2}$-$3p_{1/2}$ (fourth order)
3.9901964 ± 138 Å	Balmer δ $2p_{3/2}$-$6d_{5/2}$
3.9910155 ± 138 Å	Balmer δ $2p_{3/2}$-$6d_{3/2}$
3.9932951 ± 129 Å	Balmer δ $2p_{3/2}$-$6s_{1/2}$
4.1539315 ± 140 Å	Balmer γ $2p_{1/2}$-$5d_{3/2}$
4.1555266 ± 140 Å	Balmer γ $2s_{1/2}$-$5p_{3/2}$
4.1581985 ± 140 Å	Balmer γ $2p_{1/2}$-$5s_{1/2}$
4.1599155 ± 140 Å	Balmer γ $2s_{1/2}$-$5p_{1/2}$
4.2221619 ± 140 Å	Balmer γ $2p_{3/2}$-$5d_{5/2}$
4.2236380 ± 140 Å	Balmer γ $2p_{3/2}$-$5d_{3/2}$
4.2280495 ± 140 Å	Balmer γ $2p_{3/2}$-$5s_{1/2}$
4.3490013 ± 1500 Å	$1s2s\ ^3S_1$-$1s5p\ ^3P_2$
4.3526869 ± 1500 Å	$1s2s\ ^3S_1$-$1s5p\ ^3P_1$
4.3529965 ± 1500 Å	$1s2s\ ^3S_1$-$1s5p\ ^3P_0$
4.4055109 ± 1500 Å	$1s2p\ ^3P_0$-$1s5d\ ^3D_1$
4.4096249 ± 1500 Å	$1s2p\ ^0P_1$-$1s5d\ ^3D_2$
4.4096885 ± 1500 Å	$1s2p\ ^3P_1$-$1s5d\ ^3D_1$

TABLE III. (*Continued.*)

$^{32}Ge^{74}$ nλ	Identification
	(b)
4.4099416 ± 1500 Å	$1s2s\ ^1S_0$-$1s5p\ ^1P_1$
4.4147830 ± 1500 Å	$1s2p\ ^3P_0$-$1s5s\ ^3S_1$
4.4189782 ± 1500 Å	$1s2p\ ^3P_1$-$1s5s\ ^3S_1$
4.4687187 ± 1500 Å	$1s2p\ ^3P_2$-$1s5d\ ^3D_3$
4.4701328 ± 1500 Å	$1s2p\ ^3P_2$-$1s5d\ ^3D_2$
4.4701982 ± 1500 Å	$1s2p\ ^3P_2$-$1s5d\ ^3D_1$
4.4797448 ± 1500 Å	$1s2p\ ^3P_2$-$1s5s\ ^3S_1$
4.5033884 ± 1500 Å	$1s2p\ ^1P_1$-$1s5d\ ^1D_2$
4.5109047 ± 1500 Å	$1s2p\ ^1P_1$-$1s5s\ ^1S_0$
4.6441682 ± 176 Å	Balmer β $2p_{1/2}$-$4d_{3/2}$
4.6461525 ± 183 Å	Balmer β $2s_{1/2}$-$4p_{3/2}$
4.6546115 ± 176 Å	Balmer β $2p_{1/2}$-$4s_{1/2}$
4.6568958 ± 183 Å	Balmer β $2s_{1/2}$-$4p_{1/2}$
4.6678521 ± 28 Å	Lyman α $1s_{1/2}$-$2p_{3/2}$ (fourth order)
4.6804348 ± 20 Å	Lyman γ $1s_{1/2}$-$4p_{3/2}$ (fifth order)
4.6826112 ± 20 Å	Lyman γ $1s_{1/2}$-$4p_{1/2}$ (fifth order)
4.6895951 ± 28 Å	Lyman α $1s_{1/2}$-$2p_{1/2}$ (fourth order)
4.7278558 ± 183 Å	Balmer β $2p_{3/2}$-$4d_{5/2}$
4.7314717 ± 183 Å	Balmer β $2p_{3/2}$-$4d_{3/2}$
4.7423118 ± 183 Å	Balmer β $2p_{3/2}$-$4s_{1/2}$
4.8242243 ± 104 Å	$1s2\ ^1S_0$-$1s2p\ ^1P_1$
4.8342641 ± 104 Å	$1s2\ ^1S_0$-$1s2p\ ^3P_2$
4.8522655 ± 104 Å	$1s2\ ^1S_0$-$1s2p\ ^3P_1$
4.8535315 ± 104 Å	$1s2\ ^1S_0$-$1s2p\ ^3P_0$
4.8541430 ± 1800 Å	$1s2s\ ^3S_1$-$1s4p\ ^3P_2$
4.8631275 ± 1800 Å	$1s2s\ ^3S_1$-$1s4p\ ^3P_1$
4.8638887 ± 1800 Å	$1s2s\ ^3S_1$-$1s4p\ ^3P_0$
4.9228273 ± 1800 Å	$1s2p\ ^3P_0$-$1s4d\ ^3D_1$
4.9278887 ± 1800 Å	$1s2p\ ^3P_1$-$1s4d\ ^3D_2$
4.9280415 ± 1800 Å	$1s2s\ ^1S_0$-$1s4p\ ^1P_1$
4.9280441 ± 1800 Å	$1s2p\ ^3P_1$-$1s4d\ ^3D_1$
4.9455568 ± 1800 Å	$1s2p\ ^3P_0$-$1s4s\ ^3S_1$
4.9508220 ± 1800 Å	$1s2p\ ^3P_1$-$1s4s\ ^3S_1$
5.0001175 ± 1800 Å	$1s2p\ ^3P_2$-$1s4d\ ^3D_3$
5.0035776 ± 1800 Å	$1s2p\ ^3P_2$-$1s4d\ ^3D_2$
5.0037378 ± 1800 Å	$1s2p\ ^3P_2$-$1s4d\ ^3D_1$
5.0272224 ± 1800 Å	$1s2p\ ^3P_2$-$1s4s\ ^3S_1$

TABLE III. (*Continued.*)

$^{32}Ge^{74}$ nλ	Identification
	(b)
5.0432453 ± 1800 Å	$1s2p\ ^1P_1$-$1s4d\ ^1D_2$
5.0618810 ± 1800 Å	$1s2p\ ^1P_1$-$1s4s\ ^1S_0$
6.2332054 ± 336 Å	Balmer α $2p_{1/2}$-$3d_{3/2}$
6.2368162 ± 336 Å	Balmer α $2s_{1/2}$-$3p_{3/2}$
6.2793244 ± 336 Å	Balmer α $2p_{1/2}$-$3s_{1/2}$
6.2829888 ± 336 Å	Balmer α $2s_{1/2}$-$3p_{1/2}$
6.3759814 ± 336 Å	Balmer α $2p_{3/2}$-$3d_{5/2}$
6.3915783 ± 336 Å	Balmer α $2p_{3/2}$-$3d_{3/2}$
6.4387719 ± 336 Å	Balmer α $2p_{3/2}$-$3s_{1/2}$

detector. The beam angle α_{beam} to the spectrometer will shift wavelengths from one circle up and the other down, so the average yields a value for $\beta=v/c$ independent of the first-order shift. Off-axis radiation has a different angle of intersection α_1 with the crystal (for the same [X] position on the film). The basic diffraction relation for a fast-beam line is

$$\lambda_{inc} = \lambda_{th} \frac{[1 - \beta \sin(\alpha_1 + \alpha_{beam})]}{\sqrt{1-\beta^2}} \quad (1)$$

$$= \frac{2d}{n}\left(1 - \frac{4d^2}{n^2}\frac{\delta}{\lambda_{inc}^2}\right)\sin\theta_1 \cos\alpha_1. \quad (2)$$

The rest frame wavelength is λ_{th}; the value on the film and crystal is λ_{inc} (varying with film and crystal location); the lattice spacing of diffracting planes is $2d$, the Doppler velocity is $\beta=v/c=0.1772\pm0.0003$; the angle of the beam relative to the beam line and spectrometer is $\alpha_{beam}=(0.00\pm0.02)$ rad; the order of diffraction is n, and a correction for the refractive index is δ [17].

In-beam calibration lines with the same Doppler shifts as the Lyman lines allow the x-ray wavelength of the Lyman-α transition relative to that of the Balmer-β transition to be accurately determined [17]. The strongest Balmer line (Balmer β_1, $2p_{3/2}$-$4d_{5/2}$) can generally be used as a reference marker. Fits of individual spectral regions allow the consistent use of background levels and widths of the two Lyman α peaks and the seven Balmer-β components. Common widths were assumed for each Balmer component and similarly for the two Lyman components. Lorentzian profiles convolved with aperture functions or Voigt profiles were generally required—neither Gaussian nor Lorentzian profiles adequately represent the peak profiles. In the earlier analysis Lorentzian profiles were assumed, leading to possible asymmetric shift; Erickson was used for upper state levels for Balmer transitions, neglecting some contributions to those states.

VIII. SPECTROSCOPIC DATA BEYOND THE LYMAN-α–BALMER-β COMPARISON METHOD

The Lyman α–Balmer β intercomparison technique is an excellent relative technique for determining accurate spectroscopy and in particular $1s$-$2p$ Lamb shifts compared to $2l$-$4l'$ Lamb shifts (not negligible). The "beyond the Lyman α–Balmer β" or "full Balmer calibration" technique [17] is a natural development of the Lyman α–Balmer β comparison

TABLE IV. Summary of hydrogenic germanium and satellite intensities: 17° Si(Li) detector investigations, 10^9 counts/mC; and uncertainties as percent of total. The uncertainty for each tabulated intensity in parentheses is the percent statistical contribution.

Run (E)	Thickness (μg cm^{-2})	Ba α 1.97 keV	Ba β 2.66 keV	Ba γ 2.98 keV	Ba δ +edge 3.15 keV	$1s2p$-$1s^2\ ^1P_1, ^3P_1$ 10.62 keV	Ly α 10.62 keV	$1s3p$-$1s^2\ ^3P_1, ^1P_1$ 12.15 keV	Ly β 12.56 keV	Ly γ, δ +reset 13.25 keV	δmC; (%)[a]
25[b]	10	3.68(3.0)	0.827(7.3)	0.167(58)	0.087(47)	0.883(64)	17.6(1.4)	0.120(40)	4.70(6.8)	5.62(0.7)	14.5
26[c]	10	4.93(1.7)	0.963(6.4)	0.227(56)	0.116(450)	1.24(65)	23.6(1.7)	0.364(90)	5.55(0.4)	6.15(1.8)	14.5
20[b]	25	3.40(33)	0.845(16)			0.720(160)	26.35(0.8)		5.62(2.6)	6.41(6.7)	14
28[b,c]	25	5.18(3.4)	1.05(8.2)	0.636(143)	0.493(133)	0.193(56)	24.5(0.7)	0.023(25)	5.7 8(1.0)	6.92(1.6)	1.8
21[b]	50	6.00(7.4)	1.36(28)	0.343(135)		2.01(13)	33.0(0.3)	0.239(11)	8.12(1.1)	12.2(3.1)	2.5
22[c]	50	5.33(3.3)	0.962(5.9)	0.200(16)		1.05(9.5)	28.4(0.2)	0.085(65)	7.21(5.5)	9.88(1)	18
27[b,c]	50	4.45(2.4)	0.892(5.8)	0.351(47)	0.084(40)	1.71(28)	21.6(1.0)	0.212(32)	5.31 (0.8)	9.44(5.8)	18
23[b]	238	6.48(3.9)	0.819(32)	0.163(37)	0.074(50)	6.88(67)	80.3(5.9)	0.803(30)	15.2(1.7)	32.6(1.6)	11.5
24[c]	238	5.87(3.4)	1.04(12)	0.122(67)	0.351(147)	11.0(17)	54.7(0.7)	1.25(13)	12.7(0.5)	26.5(1.0)	11.5
29[c]	25	3.86(2.5)	0.776(6.0)	0.151(26)	0.172(67)	1.04(52)	21.4(2.8)	0.148(33)	5.64(0.4)	7.42(5.3)	1.8
ΔEff[d]	(13.5)	(6.0)	(4.3)	(3.6)	(0.1)	(0.1)	(0.1)	(0.1)	(0.1)		

[a]Uncertainty in the exposure (%); nominally 0.1 mC; but increased for a given target thickness if spectra are inconsistent.
[b]New foil.
[c]Calibrated by x-ray source after run.
[d]Percent efficiency uncertainty from Table II.

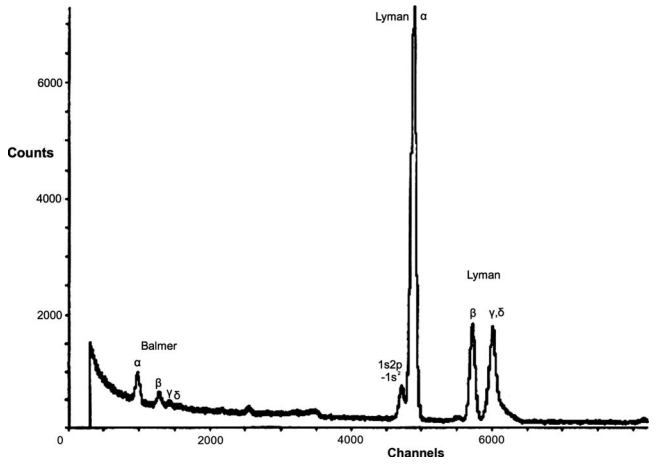

FIG. 1. Example Si(Li) detector spectrum.

method and gives a significant reduction in the uncertainty of the final result.

IX. FITTED RELATIVE COMPONENT INTENSITIES

The results for Si(Li) spectra are presented in Table IV. Results are listed in order of increasing target thickness. The 680 μg cm^{-2} carbon stripper foil yielded much higher currents and better statistics than the 400 μg cm^{-2} foil (500 versus 90–150 nA of bare ions), showing that equilibrium in stripping was not obtained with the thinner stripper foil.

Thin 10 μg cm^{-2} excitation targets provided much lower satellites and higher Balmer-to-Lyman intensity ratios. As expected, thicker target foils gave higher intensities but lower I(Balmer β)/I(Ly α) ratios and greater heliumlike contamination as the processes of capture and deexcitation of highly excited states occurred within the foils. Uncertainties arise from fitting uncertainties and backgrounds, the dead layer and other corrections, and uncertainty in exposure times. These three contributions are given separately, as percentages of the total.

Figure 1 presents a typical spectrum taken with the Si(Li) detector mounted at 17°. All heliumlike peaks are weak, and resonance satellites to Balmer transitions are unobservable. In each spectrum, the general trend of decreasing intensity with higher excitation is followed. By comparison the 90° Si(Li) spectra show relatively heavy satellite contamination from downstream metastable decays, unobservable with the 17° detector due to the collimation.

Compared to previous experiments selecting a hydrogenic Ge^{31+} incident beam, background levels are greatly reduced. A large part of the background arises from electrons ejected by the target, exciting x rays on impact with other parts of the spectrometer. Use of magnetic baffles and increased collimation prevented electrons from reaching the film holders, yielding a significant improvement in signal to background ratios. On the short wavelength end of the films, some background from bremsstrahlung is still observed, but this does not interfere with important regions of the spectra. Charge-state analysis has been conducted in relatively large detail (e.g., [1,3]), so it is known that equilibrium populations of Z=32, E=14.78 MeV/amu (β=0.1772) are given in Table V.

With bare incident charges, competing processes are one- and two-electron capture, and the former is dominant for the thin targets used herein. As thicknesses approach equilibrium values, effects of straggling and stopping-power become significant, multiple collisions lead to two-electron capture, and excitation and ionization processes become more important. The stopping range for germanium in carbon is approximately 38 mg cm^{-2}, with stopping powers of 21(1) MeV/(mg cm^{-2}) [34–36]. For the optimal 10 μg cm^{-2} targets, this slowing is much less than uncertainty in the incident beam velocity. Straggling broadens the profile symmetrically, so contributes no shift. The low intensity of the resonant heliumlike $1s2p$-$1s^2$ peak suggests that satellite contamination of hydrogenic peaks is also relatively minor.

The spectra are indeed very far from equilibrium, with Lyman α: $1s2p$-$1s^2$ ratios of 19.4:1.0($\pm$.6) for 10 μg cm^{-2} targets instead of 0.69:1.0 from equilibrium charge fractions. The population of hydrogenic and heliumlike ions might be expected to increase linearly with target thickness (or as $1-e^{-At}$ near equilibrium for some A). This is roughly observed for heliumlike states (given the exposure, fitting, and target thickness uncertainties) and may be assumed true for satellite contamination.

The Si(Li) data (Table IV) shows that Lyman α radiation increases by factors of 1.8 and 3.3 as the target thickness increases from 10 to 50 to 238 μg cm^{-2}. Conversely, Balmer β, γ, and δ radiations show *no* increase in intensity with thickness. Balmer α and Lyman β increase by factors of 1.22 and 1.34 for 10–50 μg cm^{-2} and 1.43 and 2.72 for 10–238 μg cm^{-2}, respectively, and $1s2p$-$1s^2$ and $1s3p$-$1s^2$ increase by factors of 1.50 and 1.06 and 8.42 and 6.11, though the uncertainties for the weak heliumlike peaks are significant (40%–90%) for the thin foils.

X. BEAM-FOIL EXCITATION, MULTIELECTRON TRANSITIONS, AND THE C1 AND C2 COMPONENTS OF SPECTRAL LINES

The increase with thickness for Lyman α intensities is much less than linear. This may imply that *collisional* deexcitation and ionization are dominant inside the foil. A direct conclusion is that s, p, and d states for $n>3$ are not populated within the foil. Hence excitation at the exit is dominant for higher-n states and gives a large contribution for all excited states. We call this thickness-independent contribution

TABLE V. Equilibrium charge distributions for β=0.1772 for Z=32 [1,3].

Q	32	31	30	29	28	27	26
Charge fraction (%)	5.6	25.5	36.8	22.8	7.5	1.5	0.2

to the spectra C2. A component C1 dependent on thickness in an exponential or linear manner may then be added for $n=2-3$ states, either due to (direct) excitation at the exit or due to radiation from within the thickness of the foil [16].

Application of this model suggests that Lyman α, Lyman β, and Balmer α radiations are composed of 77%, 87%, and 97.8% from a thickness-independent component C2 with 23%, 13%, and 2.2% radiations from this second C1 process, respectively, for the thinnest 10 μg cm^{-2} foil (neglecting the 238 μg cm^{-2} datum in the linear extrapolation). These estimates have uncertainties of 2%–3%.

XI. EFFECTS UPON DOPPLER ANGLE

For the C1 fraction of Lyman radiation increasing with thickness, a shift of the emission source upstream compared to that for Balmer radiation will arise if the emission location is within the foil. If emission arose from half-way through the film, the Lyman-α beam energies would be 0.11 MeV higher than Balmer β, or $\delta\beta=1.5\times10^{-5}$, giving $\delta\lambda=2$ ppm. An additional effect arises for the shift of the dispersion plane for Lyman α versus Balmer β radiation. Because of the slanted lines, this yields a Doppler shift between the radiation.

The slant of the lines on the film is approximately β, so this 11.25 μm shift upstream would give a 2.0 μm shift across the film or an effect at the 5.7 ppm level. This begins to be significant, but only applies to 23% of the radiation. It shifts Lyman α upstream, giving low Lyman α wavelengths and would be corrected for by shifting λ to larger values. Assuming a single source and uniformity of this component with thickness, it may be revealed by a trend of discrepancy with target thickness. Of course, satellite and other effects may dominate over this effect. Wake fields are believed to give negligible Stark shifts but could give a shift in relative Balmer intensities. Excitations could be from atomic interactions or at the foil exit, while Balmer deexcitation occurs in the free-field region downstream of the foil (c.f [15]).

Another contribution of the Si(Li) data is revealed by the different variation of $n=3-2$ and $n=3-1$ transitions with thickness, and their relative amplitude. For Lyman β, only p states are involved, so the Balmer variation implies that the dominant (d-p) transitions are entirely free of this C2 component (if the $3d:3p$ ratio is greater than $5.9\pm2:1$). For the thin foil, the ratio of Balmer α to Lyman β is $0.836\pm0.053\pm0.113:1.0$, where the first uncertainty is statistical and the second relates to the detector efficiency uncertainty. Subtraction of the second C2 contribution yields a relative intensity of $0.940\pm0.060\pm0.127:1.0$. Branching ratios for ($3s$,$3p$, and $3d$):$3p$ states for these transitions in free space (downstream of the target) are [1.0, 0.121(0), 1.0]:0.879(80) where slight uncertainty arises from $3p_{1/2}$ versus $3p_{3/2}$ upper levels. Coster-Kronig transitions appear negligible by comparison. $(2l+1)$ statistical population would yield a ratio of 6.36:2.64 or 2.41:1.0, in significant disagreement with the experimental value. X-rays emitted within the target are not significantly reabsorbed by the foil. For 2.0 or 2.7 keV photons (Ge Balmer α, β) and a 238 μg cm^{-2} path length, there are only 7% and 2.4% attenuations, respectively.

TABLE VI. Theoretical contributions to systematic shifts and theoretical uncertainties in the Lyman-α–Balmer-β region in Ge^{31+} for a Rowland circle radius of 300 mm. RI corrections in micrometers to observed (raw) locations on the emulsion around the Rowland circle. All results give relative shifts for fourth order diffracting Lyman-α radiation compared to those for first-order Balmer-β radiation. Variations for other peaks such as Lyman β versus Balmer δ are given elsewhere [22].

Crystal-specific parameters	Si 111 crystal
RI: infinite flat perfect crystals	-39 μm
RI: (finite crystal with focusing)	-1 μm
RI: depth penetration	-42 μm
Geometry (finite source)	-1 μm
Densitometry: emulsion penetration	$+3$ μm
High-precision shifts	$+6.3\pm0.3$ μm
Sum: Si 111 crystal	-73.9 ± 0.3 μm
cf. Balmer-β wavelength ±3.9 ppm	±1.35 μm
Contributions to uncertainties due to input parameter uncertainties	
Crystal T	±2.74 μm
α_{plane}	±1.50 μm
Polarization	$+(0.19\pm0.19)$ μm
Other (α_{beam})	±0.50 μm
Voigt fitting ($h=1.00$ mm)	(-0.11 ± 0.39) μm
Voigt fitting ($h=0.40$ mm)	$(+1.51\pm0.34)$ μm
Densitometry	±0.26 μm
Subtotal	-72.2 ± 3.2 μm

The spatial distribution of x rays is distorted by the Doppler effect. A distribution spherical in the emission frame for $\beta=0.1772$ leads to concentration factors of 1.43 in the forward direction or unity for normal incidence for all lines. The relative intensities are not affected by this variation. The variations in target thickness help to confirm the assumption that the thin foils corresponded to a single capture and excitation process. A series of multiple collisions and electron capture and ionization processes would decelerate the beam and produce predominantly helium-like and lithiumlike spectra. This satellite contamination has been a significant problem in other experiments but is conclusively ruled out by observed spectra [16]. Qualitative agreement between Si(Li) detectors supported the assumption of isotropic emission for the dominant peaks and implied that absorption of Balmer radiation by the target foil was not a significant problem.

XII. CRYSTAL DIFFRACTION AND SPECTRAL POLARIZATION

Refractive index and geometric corrections should be calculated for each line and depend on crystal type and perfection, mosaicity, and spectral polarization [17]. Tables VI and VII indicate the diffraction parameters and their uncertainty compared to spectral separations, and the consequent uncertainty in the centroid location. The first table provides mea-

TABLE VII. Summary of theoretical contributions to systematic shifts and theoretical uncertainties in the Lyman-α–Balmer-β region in Ge^{31+} in ppm of the Lyman-α x-ray wavelength. Separation of components and (diffraction) systematics. Comparison to values from earlier analysis [6,15].

Scales and parameters	ppm		
Balmer f.s. $2p_{1/2}$-$4d_{3/2} \rightarrow 2p_{3/2}$-$4d_{5/2}$	17701		
Lyman fine structure	4637		
Lamb shift (theory)	757.6		
Instrumental resolution	659		
20 μm densitometer step length	57		
Si 111 crystal parameters	Lyman α_1	Lyman α_2	[6,15]
RI: (flat crystal) fourth vs first order shift	−109.2	−109.4	−115.6
Curved crystal depth penetration	−113.2	−111.1	−12.1
Emulsion penetration	8.9	8.9	7.7
Voigt centroid—mean shift (h=1.00 mm)	-0.3 ± 1.1	-0.3 ± 1.1	$\pm 35 \pm 12$
Voigt centroid—mean shift (h=0.45 mm)	4.3 ± 1.0	4.3 ± 1.0	
Correction for polarization	-0.55 ± 0.55	-0.54 ± 0.54	
Crystal thickness T	± 7.9	± 7.8	
α_{plane}	± 4.3	± 4.3	
Densitometry	± 0.75	± 0.74	± 4
Total high-precision curved crystal shift	-208.0 ± 9.2	-205.7 ± 9.1	-116 ± 37

sures on the emulsion around the Rowland circle of the spectrometer and detector (in micrometers); the second table provides ppm uncertainties relative to the Lyman-α energy.

The refractive index (RI) correction reported elsewhere relates to infinite flat crystal diffraction only [17]. In this experiment the important correction is the systematic shift in measured position between a high-energy Lyman transition X ray (in fourth-order diffraction) and a low-energy Balmer transition X ray (in first-order diffraction). The dynamical diffraction penetration of the x-ray wavefield has been extensively discussed [32,37,38] and has important medical applications [39,40]. Uncertainties in the parameters of the experiment (crystal thickness and beam angles) are significant, while other parameter uncertainties (crystal angles and Voigt fitting precision) are minor (Table VI).

Systematic shifts in Table VI are translated into ppm of the Lyman energy in Table VII. The scales in this hydrogenic germanium measurement have Balmer component separations, $2p$ fine structure, expected Lamb shift, resolution, and 20 μm step lengths corresponding to 17701, 4636.5, 757.6, 659 ± 7, and 57 ppm, respectively.

Systematic diffraction and geometric shifts for fourth versus first order are dominated by 121.1 ppm refractive index corrections (for first-order radiation) and 90.6 ppm shifts from curved crystal penetration (for fourth-order radiation). Uncertainty in these corrections is limited by crystal thickness, angular tolerance, and several 0.9 ppm effects to 3.2 μm or shift around the Rowland circle, or 9.2 ppm of the Lyman-α wavelength or energy. As will be seen, this is a major contribution to the final error budget. Computational and fitting precision contribute at the 0.9 ppm level, which may be compared to theoretical uncertainty in the Balmer wavelengths used to model the dispersion relation (quoted as 3.9 ppm in the table but shown to be approximately 1 ppm for dominant components) and to estimated uncertainty in theory of 0.6 ppm.

Previous work used a flat-crystal estimate for the refractive index and depth penetration effects, yielding a total correction of roughly -115 ± 37 ppm instead of the current -208 ± 9.2 ppm ([6,15], p. 51). Correction of earlier analysis for effects listed here must include the large 35 and 27 ppm uncertainties for fitting simple functions to an unknown profile (this estimate was due to the discrepancy between Lorentzian and Gaussian fitted results [15], pp. 50–52). Improved linearization and profile fitting are expected to lead to tighter error analysis.

Figure 2 illustrates the photographic data. The local χ_r^2 for an individual scan was 3–6 for a strong exposure, dominated by background noise and nonlinear densitometric linearization [25–27]. The fitted components for the Lyman-α–Balmer-β spectra are illustrated in the level diagram (Fig. 3). The wavelength scale on the emulsion and with the spectrometer are determined to very high accuracy by the ancillary in-beam peaks. The accurate determination of centroids on a common scale across this large range of energy and wavelength is unique for precision QED investigations and allows numerous systematic errors to be separately investigated.

The densitometry linearization relation for energies diffracting in first order is quite different from that for energies diffracting in fourth order, particularly for strong exposures where the density range is large. Centroids are well determined, but a single linearization scheme for first-order diffraction (Balmer energies) will tend to distort peak profiles from the fourth order of diffraction. The quality of the centroid determination is relatively independent of the final local

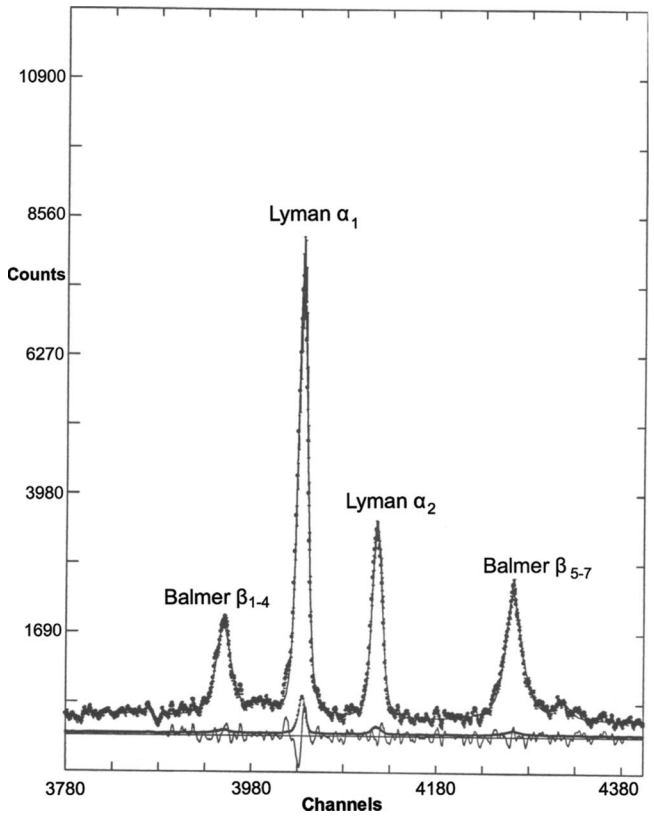

FIG. 2. Lyman-α (fourth-order diffraction) and Balmer-β (first-order diffraction) peaks fitted with Voigt profiles [(arbitrary) relative intensity versus position (channel number)]. The dots are experimental data with 1σ error bars: the line through them is the fit; the jagged line near zero is the residual: and the smooth line near zero is the densitometry 1σ error map. Theoretical input components are as given in Table III in order from left to right. On this scale, the first four Balmer components appear to correspond to the same (first) experimental peak, and the last three Balmer components appear to correspond to the last experimental peak. For this scan, $\chi_r^2=3.3$.

χ_r^2 for a single scan and well determined by the derived centroid uncertainty. The film resolution is very good, though scattered electrons from the beam and the film exposure itself provide a "noisy" background exceeding counting uncertainties. Uncertainties are reported as $\sigma\sqrt{\chi_r^2}$, where σ is the one standard deviation uncertainty.

XIII. GERMANIUM PHOTOGRAPHIC DATA AND COMPARISON TO Si(Li) INTENSITIES

The Si(Li) spectral peaks do not differentiate between different states or terms, but a valid model of the capture-excitation process should be able to reproduce experimental Balmer and Lyman ratios. Many of these ratios are given for specific transitions in the photographic data, but normalization of the Lyman to the Balmer series involves uncertainty from (a) the polarizations involved and the integrated reflectivity corrections and (b) Lyman linearization corrections. These may be checked and tested against the Si(Li) data, as given in Tables VIII and IX. Fitted areas A are converted to relative intensities using

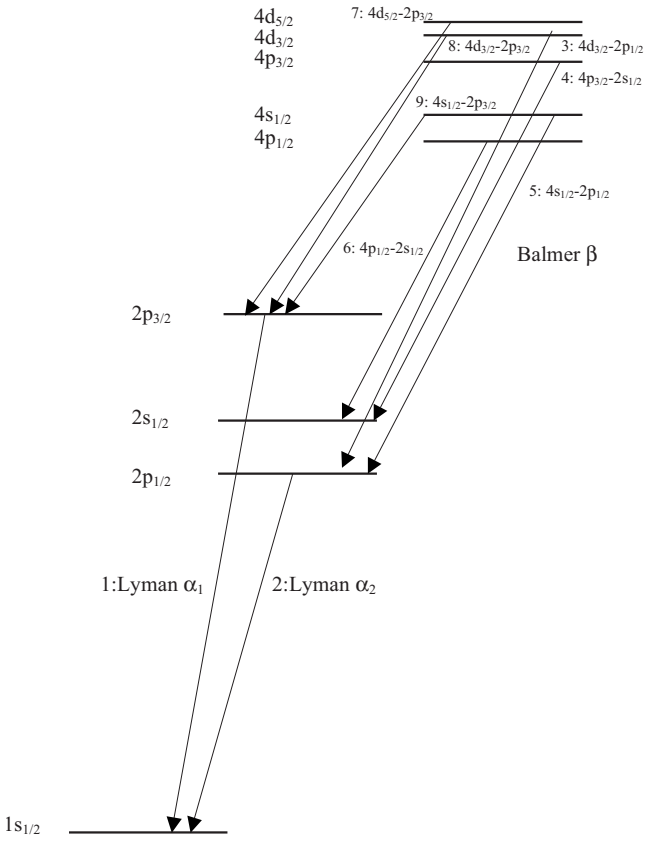

FIG. 3. Lyman-α $1s$-$2l$ and Balmer-β $2x$-$4y$ transition level diagram, labeled in order of energy.

$$I/mC(l,f)=\frac{A(l,f,c,p)}{200(0.1\mu)}\frac{\pi}{R_H^{\theta_1}(l,p,c)}\frac{2C(l,c)}{h(f)E(f)}L(l,s),$$

where l, f, c, p, and s are the line, film, crystal, polarization, and scan involved, respectively. $E(f)$ is the photographic exposure in mC, R_H is the integrated crystal reflectivity, $L(l,s)$ is the densitometry correction for the linearization of different orders, $h(f)$ is the film height used in the densitometry and linearization, and $C(l,c)=BX+S_k+S_{kin}+x_{line}$ is the mean path length from the source to the film [16,22]. The value $\frac{h(f)}{2C(l,c)}$ is (therefore) the detector solid angle. A, h, E, and C are well defined.

The densitometry linearization (for higher-order radiation) is quite different for germanium energies diffracted from silicon crystals compared to those for iron radiation diffracted from ammonium dihydrogen phosphate or pentra-erythritol crystals [17]. In the latter, the correction factor is of order unity (typically 0.4–1.5). For the current experiment, the correction factor is typically 3–5 [25–27]. This large factor has an associated uncertainty which contributes to the final uncertainty of the scaling. There is also a minor uncertainty due to the computation of R_H^{π} [41]. In particular, the higher-order germanium Lyman-γ and δ radiations lie above the Br K edge, so the linearization in this region involves an extrapolation with larger uncertainty.

TABLE VIII. Hydrogenic germanium and satellite intensities, 10 μg cm^{-2} carbon target: Photographic measurements, relative to Balmer β_5.

Line	Area (10^5 μm)	L_3[a]	R_H^π (10^{-6})	$I_{rel,\pi}$	Photo[b]	Sums[b]	I_{rel} Si(Li)[c]
1Balmer ζ_{1-4}	0.72(9)	1	110	0.059(7)	0.059		
4Ly $\gamma_{1,2}$	2.39(15)	5.19	57.8	1.93(12)(25)	3.05	3.05(44)	5.42(227)
1Balmer ε_{1-4}	0.69(5)	1	111	0.056(4)	0.056		
1Balmer ε_{5-7}	1.08(5)	1	112	0.088(4)	0.088	0.144	
1Balmer δ_{1-4}	1.20(6)	1	113	0.093(5)	0.093		
4Ly β_1	5.74(20)	4.68	60.7	4.18(15)(25)	7.03		
4Ly β_2	1.84(6)	4.69	60.7	1.34(4)(8)	2.25	9.29(61)	10.67(73)
1Balmer δ_{5-7}	1.73(9)	1	114	0.136(7)	0.136	0.229	0.198(93)
1Balmer $\gamma_{1,2}$	3.11(10)	1	118	0.233(7)	0.233		
1Balmer $\gamma_{3,4}$	0.56(4)	1	118	0.042(3)	0.042		
1Balmer $\gamma_{5,6}$	4.70(18)	1	120	0.351(13)	0.351		
1Balmer γ_7	0.39(4)	1	120	0.029(3)	0.029	0.655	0.379(220)
1Balmer β_1	7.50(25)	1	134	0.609(20)	0.609		
1Balmer β_2	1.26(15)	1	134	0.102(12)	0.102		
1Balmer β_3	0.39(7)	1	134	0.032(6)	0.032		
1Balmer β_4	0.53(10)	1	134	0.043(7)	0.043		
3Ly α_1[d]	37.7(7)	3.01	65.0	14.81(28)(71)	21.78		
3Ly α_2[d]	20.0(6)	2.97	64.2	7.84(24)(38)	11.53	33.3(17)	39.90(48)
4Ly α_1	25.3(4)	3.14	62.3	14.73(23)(68)	25.83		
4Ly α_2	12.0(3)	3.30	61.8	7.09(18)(33)	12.44	38.3(18)	39.90(48)
1Balmer β_5[d]	12.4(3)	1	137	1.000(24)[a]	1		
11Balmer β_6	1.15(30)	1	138	0.092(24)	0.092		
1Balmer β_7	0.97(5)	1	138	0.078(4)	0.078	1.956	1.876(136)
$3x1s2p\ ^1P_1$-$1s^2$	1.48(10)	3.13	59.6	0.677(46)(32)	1.028		
$3x1s2p\ ^3P_1$-$1s^2$	1.03(6)	3.13	58.7	0.480(28)(23)	0.733	1.76(12)	2.00(129)
$4x1s2p\ ^1P_1$-$1s^2$	0.92(7)	3.28	58.7	0.579(44)(15)	0.951		
$4x1s2p\ ^3P_1$-$1s^2$	0.94(9)	3.28	57.9	0.602(58)(16)	0.978	1.93(13)	2.00(129)
$4x1s3p\ ^1P_1$-$1s^2$	0.0(4)	3.27	63.4	0.0(3)			
$4x1s3p\ ^3P_1$-$1s^2$	0.0(4)	3.27	63.5	0.0(3)			0.272(109)
1Balmer α							8.345(249)

[a]C and R_H^π are consistent for different exposures, but L varies for different exposures.
[b]Sum assuming Lyman radiation is unpolarized.
[c]Reference line for normalization. Si(Li) data normed to Balmer β and Lyman α.
[d]3Ly α_1 L range: 2.2–3.134; 3Ly α_2: 2.62–3.134.

Germanium 238 μg target results are consistent with the thinner targets but the broadening and background prevent the thick-target result from being a critical measurement. The remaining germanium results are consistent, within a significant scatter. Fitted dispersion parameters do not vary smoothly and appear to contribute to this scatter. Relative intensities were only derived for Lyman-α, β and Balmer-β, δ for the original germanium analysis [15], and the method used was unreliable. In particular, profiles were not corrected for linearization in different orders and the scale used based on Henke *et al.* [42] had errors of 50%[22].

A typical Balmer-γ region is plotted in Fig. 4. Components can be seen as shoulders to the spectra. Weaker components begin to be dominated by noise, but the energy spread of the components becomes smaller so the consequence of this is minor. Individual scans have significant variance for peaks if they are fitted independently, but the consistency across scans is strong.

Lyman-β–Balmer-δ regions are of course weaker (Fig. 5). The Lyman components are now just resolved on individual scans and the residuals remain dominated by noise. In the remaining two example regions (Figs. 6 and 7), the signal to noise degrades further, especially for the Balmer peaks, but the Lyman components, though unresolved, are clear and well fitted. At this scale some grain correlation is observed. Independently, these ancillary regions provide weak determinations of QED corrections, primarily due to the relatively low exposures and hence statistical quality. χ_r^2 values are

TABLE IX. Hydrogenic germanium and satellite intensities, 50 μg cm^{-2} carbon target: Photographic measurements, relative to Balmer β_5.

Line	Area (10^5 μm)	L	C (10^5 μm)	I_{rel}, π	Photo [a]	Sums [a]	I_{rel} Si(Li) [b]
4Ly $\gamma_{1,2}$	1.48(15)	5.19	2.08	2.43(3)(25)	3.82	3.82(40)	5.20(136)
1Balmer δ_{1-4}	0.63(5)	1	2.18	0.100(8)	0.1		
4Ly β_1	4.69(10)	4.69	2.18	6.93(0.3)(42)	11.64		
4Ly β_2	1.26(6)	4.69	2.18	1.86(0.4)(11)	3.13	14.77(89)	15.70(87)
1Balmer δ_{5-7}	0.98(4)	1	2.18	0.156(6)	0.156	0.256	
1Balmer γ_{1-4}	1.53(8)	1	2.28	0.232(12)	0.232		
1Balmer γ_{5-7}	2.39(7)	1	2.31	0.362(11)	0.362	0.594	0.435(70)
1Balmer β_1	3.64(11)	1	2.51	0.599(18)	0.599		
1Balmer β_2	0.58(8)	1	2.51	0.095(13)	0.095		
1Balmer β_3	0.15(3)	1	2.52	0.025(5)	0.025		
1Balmer β_4	0.33(5)	1	2.52	0.054(8)	0.054		
3Ly α_1 [c]	42.1(13)	2.72	1.96	30.3(0.3)(15)	44.59		
3Ly α_2 [c]	22.3(6)	2.91	1.96	17.37(1)(83)	25.54	70.1(34)	61.85(11)
4Ly α_1	21.4(7)	3.16	2.53	25.19(3)(116)	44.20		
4Ly α_2	10.1(3)	3.30	2.54	12.15(1)(56)	21.31	65.5(30)	61.85(11)
1Balmer β_5 [b]	6.12(22)	1	2.55	1.000(36)	1 [b]		
1Balmer β_6	0.70(4)	1	2.55	0.114(7)	0.114		
1Balmer β_7	0.56(4)	1	2.56	0.091(7)	0.091	1.978	2.095(124)
$3x1s2p\ ^1P_1$-$1s^2$	1.59(18)	3.13	2.01	1.50(2)(7)	2.28		
$3x1s2p\ ^3P_1$-$1s^2$	1.18(16)	3.13	2.02	1.12(2)(5)	1.71	3.99(19)	2.29(22)
$4x1s2p\ ^1P_1$-$1s^2$	0.81(10)	3.28	2.60	1.03(2)(3)	1.70		
$4x1s2p\ ^3P_1$-$1s^2$	0.86(8)	3.28	2.61	1.12(1)(3)	1.81	3.51(10)	2.29(22)
$4x1s3p\ ^1P_1$-$1s^2$	0.0(4)	3.27	2.25	0.0(3)			
$4x1s3p\ ^3P_1$-$1s^2$	0.0(4)	3.27	2.25	0.0(3)			0.185(121)
1Balmer α							11.61(38)

[a]Sum assuming Lyman radiation is unpolarized.
[b]Reference line for normalization. Si(Li) data normed to Balmer β and Lyman α.
[c]High background and asymmetry in third-order profiles 3Ly α_1 L range: 2.2–2.91; 3Ly α_2: 2.682–2.985.

typically 3–6. However, as mentioned before, the wavelength scale on the emulsion and with the spectrometer are determined to very high accuracy by these ancillary in-beam peaks.

The best data for 10 and 50 μg cm^{-2} thicknesses are presented in Tables VIII and IX, comparing experimental measured peak areas to derived normalized relative intensities emitted at the source I_{rel}, assuming π polarization, and to the sums of these for particular multiplets (e.g., Balmer ϵ and Lyman β). The tables compare these sums from the photographic data to the derived Si(Li) detector intensities.

Normalization is a significant issue. In considering variation in a particular component with thickness, it is important to normalize to a component believed free of this effect. For the photographic data, Balmer β_5 is a good candidate for this and is the strongest component in the strongest Balmer multiplet. Hence this normalization is the most sensible for this comparison. Below we discuss the relative model dependence of high-n peaks and for this a comparison or normalization with Balmer δ is preferable. For the Si(Li) data, the strongest and best-defined transition is that of Lyman α, so normalization to this is most sensible. However, for the comparison of normalization schemes from the Si(Li) data to the photographic peak, there are choices. Normalizing to the Balmer-β_{5-7} peak is consistent, but the Si(Li) accuracy of the Balmer series is relatively poor. We expect that all peaks will either stay the same or increase with thickness, mainly determined by the significance of the C2 (thickness-independent) component to the data. However, normalizing to the Balmer-β_{5-7} peak leads to the Lyman-γ peak decreasing with thickness (unlikely in the thin-foil interaction region). Conversely, normalizing to Lyman α yields peculiar (false) apparent changes of (all) Balmer lines with thickness. Hence we normalize to Balmer β_{5-7} and Lyman α simultaneously and discuss results.

The 14%–20% scatter between Si(Li) measurements with the same target thickness illustrates the scale of background and fitting uncertainties. Two important pieces of data are provided by the Si(Li) data, in addition to general confirmation of linearity and relative intensities. Comparison of Balmer β to Lyman α is given more critically by the Si(Li)

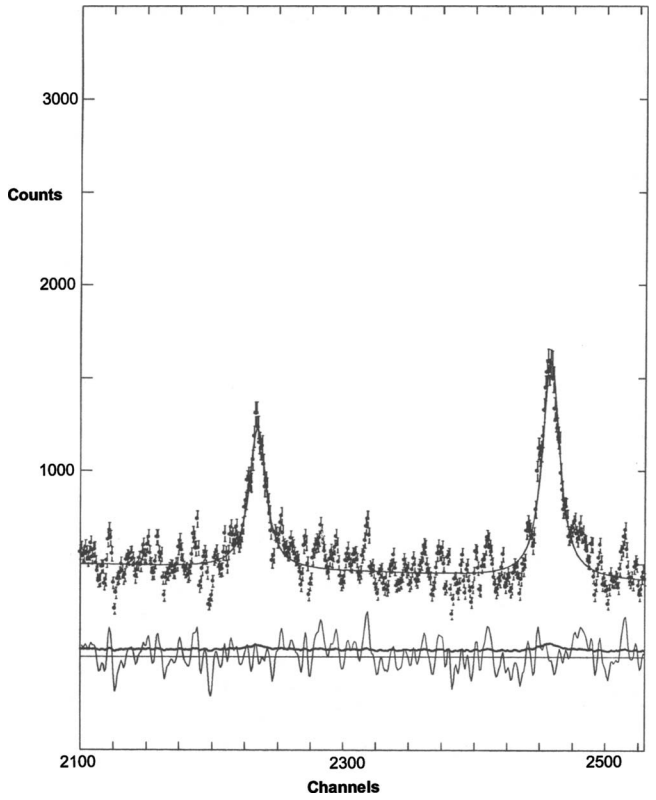

FIG. 4. Balmer-γ-region $2l$-$5y$. The curves have the same meaning as in Fig. 2. Noise dominates over the residuals. Theoretical input components are as given in Table III in order from left to right. On this scale, the first four Balmer components appear to correspond to the same (first) experimental peak, and the last three Balmer components appear to correspond to the second experimental peak. For this scan, $\chi_r^2=4.2$

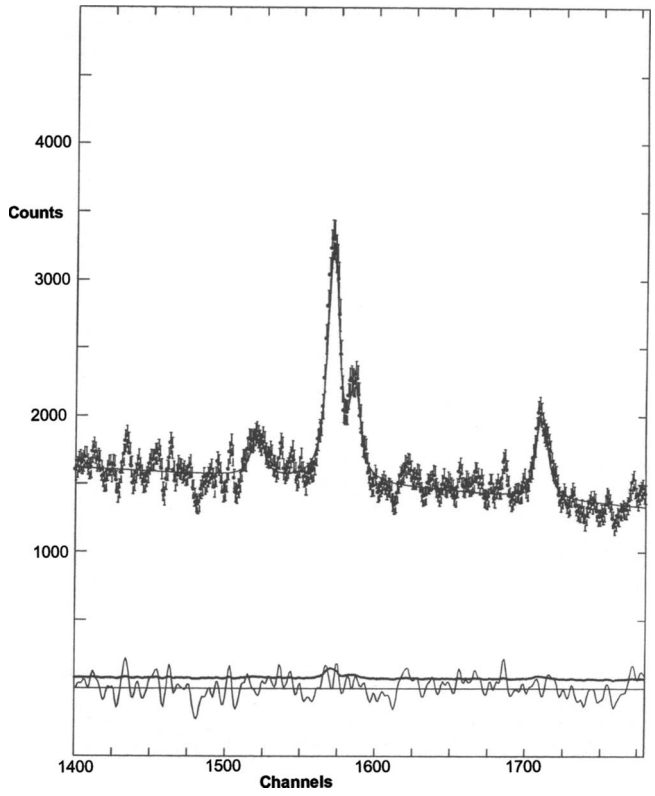

FIG. 5. Lyman-β $1s$-$3l$ (fourth-order diffraction) and Balmer-δ region $2x$-$6y$ (first-order diffraction) fitted with Voigt profiles [(arbitrary) relative intensity versus position (channel number)]. The dots are experimental data with 1σ error bars; the line through them is the fit; the jagged line near zero is the residual; and the smooth line near zero is the densitometry 1σ error map. Theoretical input components are as given in Table III in order from left to right. The first four Balmer components appear to correspond to the same (first) experimental peak, and the last three Balmer components appear to correspond to the last experimental peak. The two Lyman components are clear and well fitted but less well resolved. The Lyman-Balmer technique works in all orders.

results and Balmer-α wavelengths are particularly provided by the Si(Li) detector data.

The Balmer series then agree well for the two detection systems, and relative intensities of third- and fourth-order diffractions of the same lines are also in remarkable agreement. Lyman-α component ratios are almost precisely 2:1 (statistical) when valid linearization is used. Lyman-β ratios ($1s$-$3p_{3/2}$-$1s$-$3p_{1/2}$) are $3.02\pm.14:1$ and $3.61\pm.17:1$ by contrast.

The increase in low-n radiation (from 10 to 50 μg cm^{-2} thickness) is clear in the photographic data, as it was for the thick target Si(Li) data but with much higher accuracy. Lyman α, β, and γ increase by ratios of 1.70, 1.59, and 1.26 compared to Balmer β (or raw ratios of 1.59, 1.49, and $1.18\pm.10$ without normalization for solid angles and densitometry). Corresponding Si(Li) values for Lyman α and β are in good agreement. Similarly, heliumlike resonance transitions clearly increase with thickness as expected for the required multiple-excitation process. Results show an increase with thickness in $2s$-$4p$ and $2p$-$4s$ radiation compared to $2p$-$4d$ of 2.8% and 5.5%, below standard deviation uncertainty but contrasting with a $1s$-$4p$ increase of 18% above.

An average of $2s$-$4p_{3/2:1/2}$ (Balmer β_2: Balmer β_4) doublet ratios and $2p$-$4s$ doublet ratios (Balmer β_7:Balmer β_3) over the two films gives $2.03\pm0.37:1$ and $2.96\pm0.52:1$, respectively, in reasonable agreement with statistical 2:1 values. The three $2p$-$4d$ components (Balmer β_6:Balmer β_1:Balmer β_5) separately give ratios of $0.83\pm0.22:5.48\pm0.2:9.0\pm0.2$ and $1.03\pm0.06:5.39\pm0.2:9.0\pm0.3$ for the two different thicknesses, also in good agreement with statistical 1:5:9 ratios. The $2p_{1/2}$-$4d_{3/2}$ component may be nonstatistical, arising from overlap with the $2s$-$4p_{1/2}$ component, but the discrepancy is only at the 2σ level. The largest shift between the components in the photographic data is that of the $\frac{3}{2}$-$\frac{3}{2}$ intensity contribution, correlated to the strong peak and only at the 1σ level.

In summary, the photographic data are in excellent agreement with the Si(Li) data with three exceptions. Third-order Lymam α is very strong and variable and hence the linearization factor is relatively uncertain. In the thicker foil, there is also high background and asymmetry for third order lines. For the thin target, the third-order Lyman-α intensity in the photographic linearization is some three standard deviations lower than the Si(Li) intensity; the thicker target has this same intensity too high by some three standard deviations,

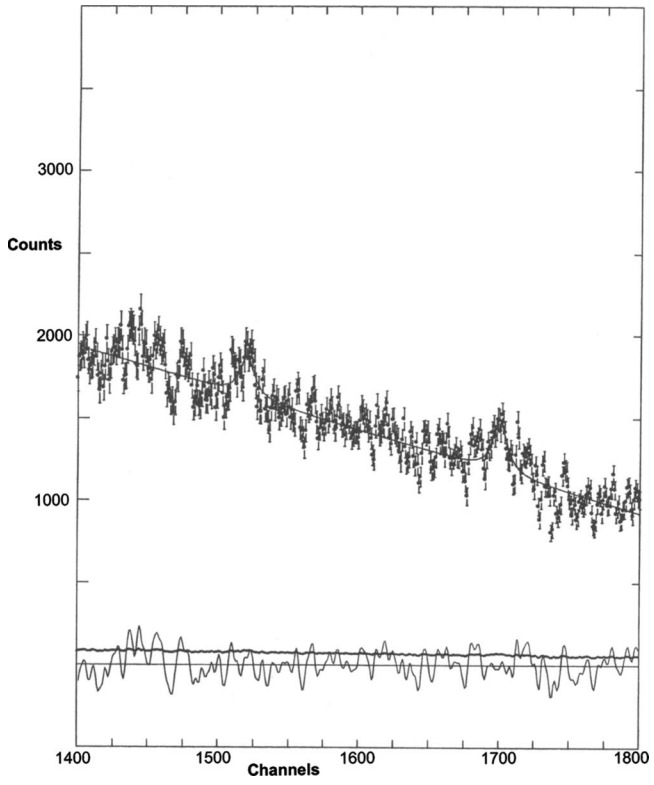

FIG. 6. Balmer-ε region $2l$-$7y$. Note in this scan the relatively poor signal to noise and sloping background.

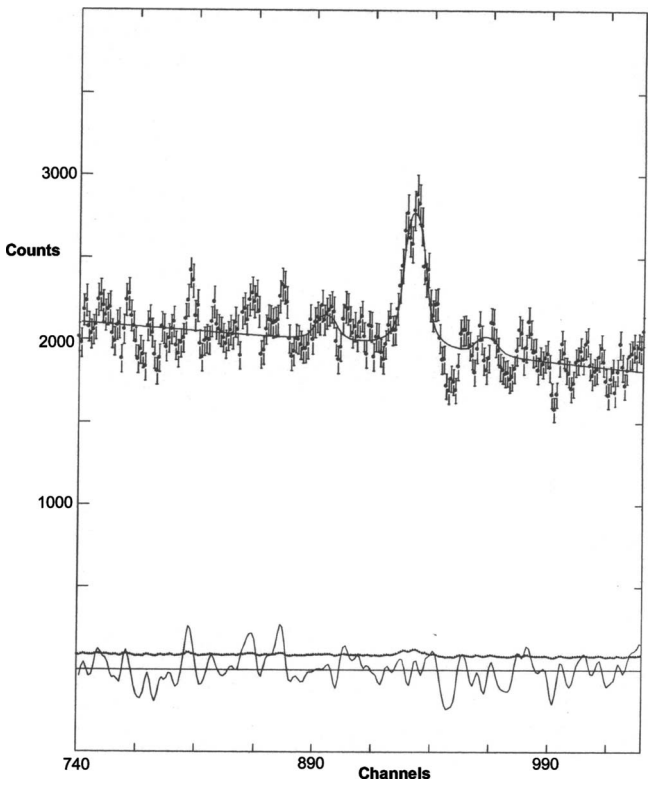

FIG. 7. Lyman-γ $1s$-$4l$ and Balmer-ζ region $2x$-$8y$. For these high-n transitions, on individual scans the signal to noise is unsurprisingly lower but there remains strong consistency across all scans.

and the weak heliumlike lines, in good agreement in the thinner target, are discrepant in the thicker target where the third-order lines also have a high background.

Forbidden transitions are not dominant in these spectra despite their rapid increase with Z. Neglecting the forbidden transitions, branching ratios from $4d$ and $4s$ states to $2p$ states are 0.744 and 0.586, respectively. Branching ratios for Lyman γ versus $2s$-$4p$ transitions (i.e., from $4l$ states) are 0.837:0.120.

Hence statistical population of $4l$ levels would give intensity ratios of Lyman γ:$2s$-$4p$:$2p$-$4s$:$2p$-$4d$ of 1.15:0.165:0.267:1.70. Clearly nonstatistical observed values are 1.96(12):0.143(20):0.110(10):1.70(7) and 2.46(25):0.149(21):0.116(15):1.71(6) for the two films. Si(Li) detector results would suggest an even higher value for Lyman γ, although with uncertainty due to the relative normalization. However, decays to the ground state are more probable and decays from $4s$ levels are weaker than a statistical model would predict.

Linear Stark mixing of s-f states with statistical populations might give apparent ratios for Lyman γ:$2s$-$4p$:$2p$-$4s$:$2p$-$4d$ of 2.62:0.020:0.73:0.82 [43]. Weak mixing could explain some increase in Lyman γ and an observed decrease in $2s$-$4p$ intensities but does not appear to explain the decrease in $2p$-$4s$ intensities. A mixture of Stark effects do not explain the $2p$-$4s$ versus $2p$-$4d$ ratios, which are most probably due to selective population mechanisms. In particular, the strength of Lyman spectra imply cascade contributions as discussed below. The germanium Lyman-α and Balmer-β spectra are consistent with the assumption of statistical intensities, but this is not true for higher members of the Lyman series, and those nl intensity ratios are nonstatistical.

Polarization of spectral lines

Comparison of Lyman intensities to Si(Li) detector results [6,15,22] suggests that photographic detection observes roughly half of the Lyman radiation (relative to Balmer intensities). Detailed linearized profile analysis [22,26,41] concluded that Balmer-β (i.e., nd-$2p$) radiation was significantly π polarized; it is consistent then that Lyman radiation appears to be unpolarized [16,44]. This is supported by observations in the literature [45] and by a range of models. The Bragg angle for the Lyman-α–Balmer-β region is about 49°. If the Lyman radiation is isotropic as expected, then the Si(Li) detector sees both polarizations but the crystal diffraction primarily sees only the π polarization. Within the Lyman series this factor would be almost identical for Lyman α and Lyman β. Anomalies between Lyman series are partially addressed by a ratio of $1+|\cos 2\theta|$ polarization factors (e.g., 1.14 for fourth-order Lyman α at 49°, or 1.36 for third-order Lyman α at 34°, and 1.27 for fourth-order Lyman γ at 37°).

XIV. SATELLITE RELATIVE INTENSITIES

Germanium results for the 10 μg cm^{-2} targets give ratios for the resonant satellite transition $1s2p\ ^1P_1+^3P_1$-$1s^2$ and

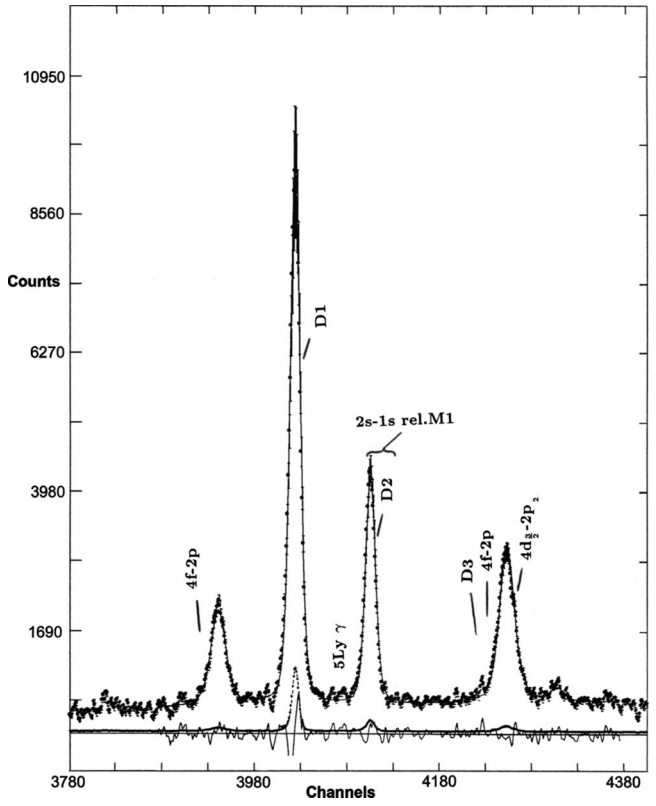

FIG. 8. Lyman-α $1s$-$2l$ and Balmer-β region $2l$-$4y$ with rough locations of potential satellites labeled. Note anticipated locations of $4f$-$2p$, $2s$-$1s$, Lyman-γ (in fifth order), and principal dielectronic satellites $2pnl$-$1snl$ to (D1) Lyman α_1, (D2) Lyman α_2, and (D3) Balmer β_5.

$1s3p\ ^1P_1+^3P_1$-$1s^2$ intensities relative to Lyman α of $5.1\pm2.3\%$ and $1.1\pm0.4\%$. The nearest doubly-excited satellites to Lyman α_1 are $2p^2\ ^1S_1$-$1s2p\ ^3P_1$ and $2s2p\ ^1P_1$-$1s2s\ ^3S_1$ as indicated in Fig. 8 [46] (D1). The $n=2$ long-wavelength satellite is relatively close to Lyman α_1 (and hence not resolved), so a 2–4 ppm shift to longer wavelength is possible for 10 μg cm^{-2} targets. Closest $n=3$ satellites are $2s3d\ ^1F_3$-$1s3d\ ^1D_2$ and $2p3p\ ^1D_2$-$1s3p\ ^3P_2$ and may give shifts at the 1 ppm level [48].

Closest satellites to Lyman α_2 with lower autoionization rates are $2p^2\ ^1S_1$-$1s2p^1P_1$ and $2s2p^1P_1$-$1s2s\ ^1S_0$ (D2 in Fig. 8). Lyman α_2 may be shifted by 4–8 ppm for 10 μg cm^{-2} targets, increasing linearly for 25, 50, and 238 μg cm^{-2} targets to 10–20, 20–40, and 95–190 ppm. These upper estimates are limited by considering trends of discrepancies with thickness. Fourth-order satellites with different diffracting crystals are observed to be negligible, or at least one order of magnitude smaller than these generous estimates [16]. Estimates based on thick 238 μg cm^{-2} targets of 100 ppm [15] (pp. 53 and 65) correspond to <4 ppm effects for 10 μg cm^{-2} targets. Additionally, the strongest $2p^2$ transitions are separated peaks, observed at the $0.6\pm0.3\%$ level. Consistency of those data sets implies that corresponding *satellite* transitions (above) are weaker by a factor of 5–10. Satellite shift estimates for 10 μg cm^{-2} targets in the germanium experiment are therefore $+1\pm1$, $+2\pm2$, ±0.3, and $+0.1\pm0.1$ ppm for Lyman-$\alpha_{1,2}$ and Balmer-$\beta_{1,5}$ radiations, respectively.

Two-photon 2-$1s$ radiation will be diffracted in second order in the Lyman-α region, as will the relativistic M1 component in fourth order. These have been discussed [49]. Estimates for the influence of these [16] yield a possible 2.7 ppm shift to shorter wavelengths for Lyman α_2 only for a 10 μg cm^{-2} target. Populations and downstream decay (below) amplify these estimates to −17 ppm.

Lyman γ in fifth order is also diffracted to the Lyman-α region, lying between the two components. Refractive index shifts are nearly identical for the two orders, so their locations in germanium spectra are 0.581 and 0.6804 times the Lyman-α separation. The weakers $4p_{1/2}$-$1s$ component is well resolved from Lyman α_2 ($\frac{\lambda}{\Delta\lambda}<671$). Expected intensities may be estimated from fourth-order Lyman-γ intensities, scaled by relative diffraction efficiencies to give $\frac{I(5\mathrm{Ly}\gamma_2)}{I(4\mathrm{Ly}\alpha_2)}\simeq1.71\pm0.25\%$ for Si 111 diffraction. This is in good agreement with observation of these peaks [24] and observation of background fitting in iron data [16] and residuals for germanium data (Fig. 8). Since peaks are well resolved, this might give a shift roughly as the square of the contamination (i.e., not linearly) and is negligible.

Estimates of $4f$-$2p$ E2 transitions based on $(Z\alpha/n^2)^2$ scaling would expect branch fractions of 0.554% for Ge, or 1.179% for [50] ([51] p. 184; [52] p. 256). Given experimental uncertainty, theoretical values will be used, but the uncertainty is then equal to the estimate. The $4f_{5/2}$-$2p_{1/2}$, $4f_{7/2}$-$2p_{3/2}$, and $4f_{5/2}$-$2p_{3/2}$ components lie 748.8, 378.2, and −1.354 ppm to the short wavelength side of the two main iron $4d$-$2p$ components [30]. These shifts are partially resolved for the strong components with $R=1335$ and 2644, respectively (Fig. 8). Shifts are strongly affected by the Yrast contribution to Balmer α and Lyman α. Intensity ratios follow expected sum rules and are 7:12:2 in field-free decay. Experimental $4d$-$2p$ ratios show larger $4d_{3/2}$-$2p_{1/2}$ intensity than expected, consistent with contamination of $4d$-$2p$ with $4f$-$2p$. The ratio of $2p_{3/2}$ to $2p_{1/2}$ is the same in both cases. Experimental d-p ratios are strongly film dependent for thin targets, and the uncertainty is larger than the difference between statistical ratios. The largest satellite shift uncertainty is therefore due to $2s$-$1s$ and $4f$-$2p$ contributions.

XV. CASCADES AND POPULATION MODELS

Some useful models for the processes of capture, ionization, excitation, and deexcitation (radiative and nonradiative) have been developed [43,45,53–74]. Capture and ionization depend on accurate atomic form factors, especially for profile asymmetries [53,75,76].

In particular, radiative electron capture cross sections may be calculated following Pratt [55–57] for bare and heliumlike [58] projectiles, nonradiative electron capture cross sections may be calculated using the eikonal approximation [59,60], the second Born approximation [61], and other approximations (e.g., the strong potential Born, impulse, and continuum distorted wave methods [24]), radiative deexcitation cross sections are well known [43,63,64], ionization calculations may be made [53,55,65–71], and estimates for collisional excitation cross sections may be computed [55,65]. The effect of cascades [64] and wake fields [45,72,73] may also be

incorporated into a suitable model. These may be used in the analysis of experimental intensities, possibly with modification for the appropriate energy regime.

However, a detailed study has shown that in this relativistic decay regime, there is prompt emission in the foil or at the target exit (thickness-dependent C1 component) and field-free decay downstream of the target (C2 component). The C1 component is indicative of multiple interactions dominated by inner-shell transitions with small radii, and the C2 component corresponding to the single interaction regime can be dominated by Yrast transitions from high-n Rydberg states [16].

The location upstream of Lyman radiation emitted within the target was mentioned earlier. If the remaining component (independent of thickness) is emitted at the same location as the Balmer β radiation, relative lifetimes lead to shifts of the dispersion plane location w_0 by $\beta\gamma c\Delta\tau$, or a mean shift along the film of $\beta^2\gamma c\Delta\tau$. For Si diffraction, the Lyman α region yields a 2.87 ppm shift in wavelength per micron along the film. Thus with $\tau_{\mathrm{Ly}\alpha}=1.460\times10^{-15}$ s $(Z=32)$ and $\tau_{4s,4p,4d}=(63.19,11.32,33.3)\times10^{-15}$ s $(Z=32)$, effective shifts defined by $4d$ versus $2p$ values will be 0.30 μm or 0.87 ppm for Si diffraction. Conversely, any free decay of the $2s$ state will incorporate shifts of 851 μm or 2440 ppm (limited by the observation length) for the observed fraction in the Lyman-α_2 component. More importantly, if the Lyman or Balmer lines arise predominantly from high-n cascades, the production location w_0 of either or both may be shifted downstream and give systematic shifts of this order. It is essential to understand the fraction of decays occurring promptly versus the component produced after cascaded decay and to estimate the n level of the initial production. To quantify this, we model six different assumptions to consider the high-n and Yrast cascades compared to the low-n production and present the comparison in Table X. Two extremes of functional dependence of the decay locations of components are given in Figs. 9 and 10.

The second component C2 is modeled with a field-free (radiative) E1 decay model following [77], modified to include $2s$-$1s$ 2-γ and $4f$-$2p$ E2 decays, and to allow population models [M0–M6 being statistical, Yrast (Fig. 9), Oppenheimer-Brinkman-Kramers approximation (OBK), mixed, $m_l=0$, $l=0-2$, and statistical including cascades, respectively (Fig. 10)] following [16]. These models cover particular lj population extremes. M0 is poor, especially for Lyman ratios, showing the significance of cascade contributions. M1 is a highly asymmetric high-l population model (pure Yrast cascade), also far from the experimental situation, seen from the vanishing higher-n Balmer relative intensities. Cascades up to $n=14$ were included; above this level contributions with $l>6$ within the observation length are negligible. Typical scales are given in Table XI. *Direct* population of $4f$ or $4d$ by, e.g., $15g$ or $15f$ have long decay lengths: these can be summed and have a minor contribution in a statistical distribution.

Decays appear to be field-free, so discussions of inconsistencies between models and experiment imply differences in initial population models. The iron analysis implied that these models underestimated contributions from cascades to Lyman α by about a factor of 2 [16]. Cascade emission locations are far downstream compared to the low-n population feeding of $2p$, implying a Doppler shift of the detected location. Models for germanium (e.g., M2 and M3) support the conclusion. Table XI contains explicit data on relative intensities (and hence populations) from $2p$, $3p$, $4p$, $5p$, $4s$, $5s$, $4d$, $5d$, $6d$, $7d$, and $8d$ states and on feeding transitions to $1s$, $2s$, and $2p$.

M2 gives the sharp $l=2$ peaked distribution, representing the standard reference model [continuum distorted wave (CDW) and peaking impulse approximation (PIA) [45]]. This OBK model requires modulation as in recent theoretical development but might be considered far superior to M3, M4, M5, and M6. It is not. It underestimates higher-n Lyman intensities and overestimates higher-n Balmer intensities, representing an overestimate of d states compared to p (and high l). It fails in the high-n region and implies that classical $l=2$ peaking is not significant for higher n states. This approximation has value in lower n shell populations but is not relevant for cascades and significant downstream decay shifts.

In the high-n region, the remaining models divide sharply: M3 gives the monotonic statistical ratio but with increased effect due to the higher relative high-n populations; M4 gives an l-independent distribution; M5 includes low-l "direct" cascades only, which are a small contribution to the total for low levels; and M6 gives the monotonic statistical ratio. M3 overestimates intensities above $n=5$ by a factor of around 2, similar to that for iron [16]. This is an indication that the n^{-2} region is not valid *per se*—if we normalize all intensities to the (weak and less well determined) Bamler-δ_5 intensity, we note that M3 is then identical to M6 in the high-n region. Hence the n^{-2} dependence is not valid for $n=5$ states, and that n^{-3} dependence *is* approximately valid at least down to $n=4$ in these regimes. Conversely, M6 underestimates these same intensities by about a factor of 1.5–2, implying at least some enhancement of the lower populations.

M4 predicts intensity ratios in disagreement with both experiments [17] and overestimates high-n intensities by 50%–100%. Lyman components are not of equal intensity and Lyman and Balmer branching ratios are incorrect. There is a tendency for the Balmer 1–4 components to be overestimated by a factor of 2.5, while the Balmer 5–7 components are overestimated by approximately a factor of 1.5, inconsistent with renormalization of intensities. Branching ratios follow a field-free decay model, subject to uncertainties, implying (again) that strong Stark or wake fields are not observed. Such fields might exist but are not strong enough to have a significant effect in this regime. The $m_l=0$ level population mechanism is not dominant for medium or high n.

The purpose (of this model investigation for germanium) is not to discover the excitation model as one of these models, which may vary from one extreme to another from low to high n states but to understand the downstream decay pattern and to isolate contributing processes. M5 and M6 are both statistical models and both match the relative intensities in the higher-n transitions moderately (much better than M0, M1, M2, and M4) and hence can be seen to approximate the cascade dependence. M6 tends to represent Balmer β ratios better, while the raw values of M5 seem to agree better for the high-n states. M3 only changed the population of lower-n

TABLE X. Hydrogenic Ge intensities relative to Balmer β_5: experiment versus modeling, 10 μg cm^{-2} target. Models M0, M1, and M2 are strongly "disproven" by the data of C1 and C2; these are presented to demonstrate regions of validity of these models. C1: thickness-dependent components (experimental). C2: thickness-independent components (experimental). M0: result of statistical population, free decay, and neglecting cascades. M1–6: models in text, including cascades (statistical, m_l=0, l=0–2, l=$n-1\rightarrow n-3$, $n^{-2,-3}$, and OBK).

	Experimental		Model predictions						
Line	C1	C2	M0	M1	M2	M3	M4	M5	M6
Ly δ	0	1.5(10)[a]	0.5635	6×10^{-8}	0.8402	0.2566	0.7036	0.3987	0.2840
Ba ζ_{1-4}	0	0.059(20)	0.0038	6×10^{-28}	0.1127	0.0481	0.0507	0.0202	0.0151
Ly γ[b]	0.19(52)	2.85(52)	3.412	0.9172	1.778	0.6528	1.849	1.291	0.9286
Ba ζ_{5-7}	0	0.00(10)	0.0036	1×10^{-28}	0.1194	0.0717	0.0541	0.0296	0.0225
Ba ϵ_{1-4}	0	0.056(4)	0.0111	2×10^{-18}	0.1727	0.0984	0.0907	0.0406	0.0309
Ba ϵ_{5-7}	0	0.088(4)	0.0106	4×10^{-19}	0.1838	0.1479	0.0979	0.0595	0.0464
Ba δ_{1-4}	0	0.0965(35)	0.0387	1×10^{-9}	0.2844	0.2282	0.1800	0.0914	0.0717
Ly β_1[b]	1.15(43)	5.88(43)	23.56	2.990	2.572	1.647	3.559	4.028	3.006
Ly β_2[b]	0.22(36)	2.04(24)	11.74	1.501	2.313	0.8312	3.226	2.026	1.512
Ba δ_{5-7}	0	0.146(10)	0.0375	5×10^{-10}	0.3048	0.3476	0.1981	0.1350	0.1091
Ba γ_{1-2}	0	0.233(7)	0.1423	0.1372	0.4469	0.1870	0.3074	0.2004	0.1696
Ba γ_{3-4}	0	0.042(3)	0.0298	8×10^{-9}	0.0718	0.0243	0.1103	0.0430	0.0305
Ba γ_{5-6}	0	0.357(6)	0.1663	0.2704	0.5392	0.3193	0.3593	0.3186	0.2798
Ba γ_7	0	0.029(3)	0.0045	1×10^{-16}	0.0228	0.0223	0.1150	0.0448	0.0317
$4f_{5/2}$-$2p_{1/2}$			0.0022	0.0075	0.0014	0.0125	0.0072	5×10^{-6}	0.0074
Ba β_1	0	0.604(5)	0.5861	0.5611	0.8135	0.5614	0.8021	0.5607	0.5611
Ba β_2	0	0.099(4)	0.3297	0.0885	0.1334	0.0629	0.1389	0.1245	0896
Ba β_3	0	0.029(4)	0.0146	2×10^{-8}	0.0333	0.0369	0.1924	0.0937	0.0661
Ba β_4	0	0.049(6)	0.1637	0.0441	0.1234	0.0315	0.1283	0.0622	0.0447
Ly α_1[b]	4.59(106)	21.24(106)	674.8	36.03	13.45	18.97	31.86	41.84	39.43
Ly α_2[b]	2.22(56)	10.23(56)	332.7	18.05	11.55	9.603	27.65	20.99	19.74
$2s$-$1s$			0.0056	4.038	0.7478	1.088	5.571	5.343	3.782
$4f_{7/2}$-$2p_{3/2}$			0.0049	0.0175	0.0024	0.0289	0.0135	1×10^{-5}	0.0173
$4f_{5/2}$-$2p_{3/2}$			0.0007	0.0021	0.0004	0.0036	0.0021	3×10^{-6}	0.0021
Ba β_5	0	1.00(3)[c]	1.0	1.0	1.0	1.0	1.0	1.0	1.0
Ba β_6	0	0.103(11)	0.1109	0.1061	0.1539	0.1062	0.1517	0.1061	0.1061
Ba β_7	0	0.085(7)	0.0275	3×10^{-8}	0.0631	0.0697	0.3639	0.1771	0.1251
Ba α	0.3(2)	9.4(5)	27.91	15.78	6.447	15.06	15.90	12.31	15.30

[a]Si(Li) detector results.
[b]Lyman intensities scaled by 2× for polarization correction.
[c]Reference line for normalization.

states compared to M6 and overestimated higher-n intensities, while M6 underestimates these same intensities. As M3 has a lower initial population of low-n states, the emission location is further downstream and more dominated by the cascade contributions. Hence some decrease in lower state populations from M6 towards M3 will yield intensities in moderate agreement with the data. For corresponding iron data [16], neither required renormalization to Balmer δ_5 to compare the higher-n and cascade dependences (and the data was more comprehensive). For the germanium data here, M6 requires renormalisation to Balmer δ_5 to make clean comparisons, requiring an increase in intensities by about 35%.

With both models, the greatest discrepancies for high n lie with Balmer $\varepsilon_{5-7}7d/s$-$2p_{3/2}$ (0.062 versus observed 0.088), Balmer $\gamma_7 5s$-$2p_{3/2}$ (0.042 versus observed 0.029), and Balmer $\beta_{1,2,3,5,7}$. Some of these details point to model deficiencies, but they indicate the pattern of decays and hence give limits for the shifts due to decay location. Cascade contributions from high-l populations (following the M1 model) are only observable in Balmer γ (and lower n) transitions and are dominated by the $6f$ and $5d$ populations. M1 also only includes pure Yrast decays versus immediate collapse modes included in M6. M6 and M1 are consistent with Yrast observations [50], and direct cascades (from M5) account for 4% of the total, suggesting near-statistical l-state distributions especially in the high-n states.

Subject to fitting uncertainty, the typical shift in expected decay length between Balmer components is approximately

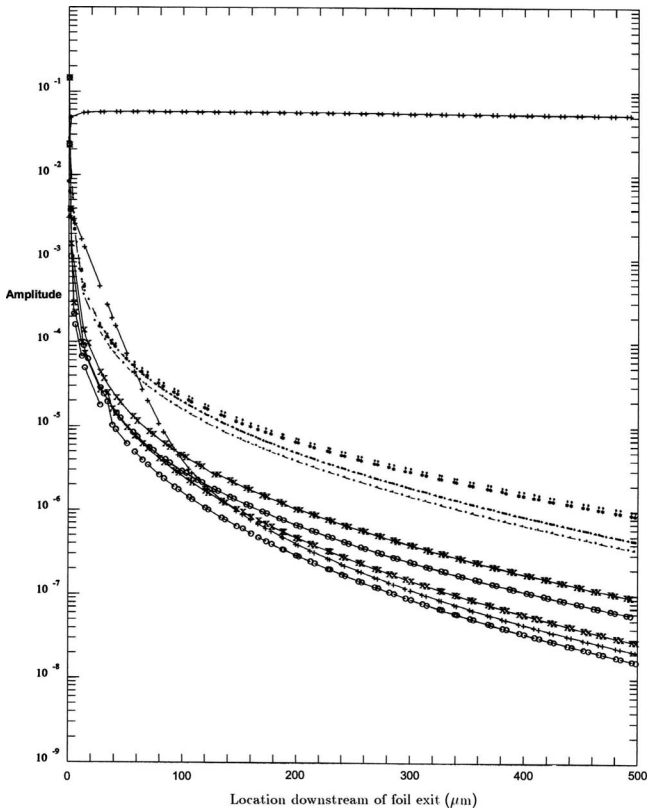

FIG. 9. Downstream populations of $4l$ and $2l$ states, and hence decay patterns for $2l$-$1s$ and $4l'$-$2l$ transitions, following model M1 in the text (population of $l=n-1,n-2,n-3$ states only, including cascades—i.e., almost pure Yrast cascades by capture into high-l Rydberg levels). Full lines indicate $2l$ populations (+ for $2s$; x for $2p_{3/2}$; and o for $2p_{1/2}$). Dashed lines with the same symbols are the corresponding $4l$ states, leaving the small-dot, dot, dot-dot-dash, and dot-dash for $4f_{7/2}$, $4f_{5/2}$, $4d_{5/2}$, and $4d_{3/2}$ populations, respectively.

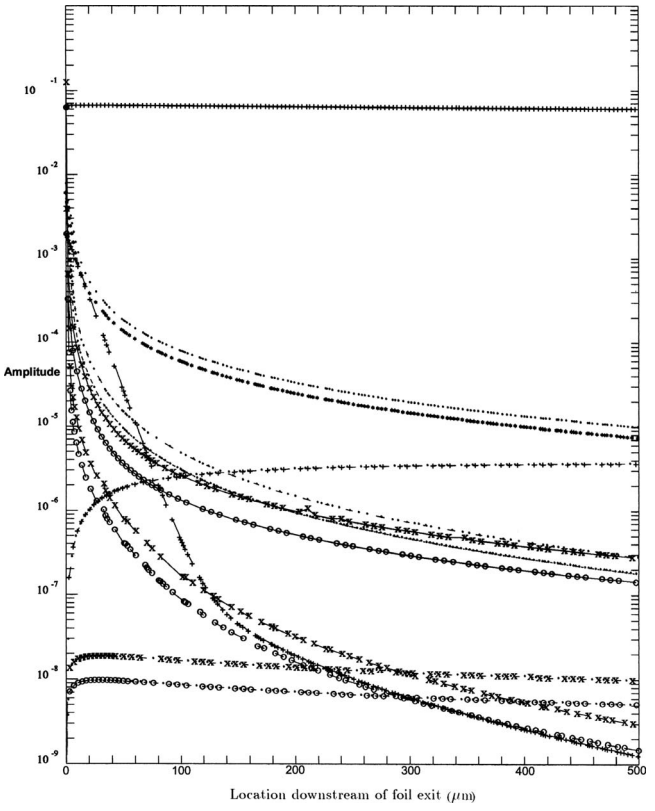

FIG. 10. Downstream populations of $4l$ and $2l$ states, following model M6 (statistical distribution including cascades up to $n=14$ in free-field decay). Perhaps surprisingly, the populations show complex increases and decays as multiple-level cascade contributions fill states before they too decay. Also, perhaps surprisingly, this statistical model gives stronger agreement with experiment than a series of other, more complex, and more developed models. Finally, disagreements of this model with experiment are observed for low-lying $2l$, $3l$, and $4l$ states as discussed in the text.

20 μm, corresponding to a 10 ppm apparent energy shift (Table XII). Separations in energy are 3000 ppm between Balmer δ_5 and Balmer δ_7 or 760 ppm between Balmer δ_5 and Balmer δ_6 so component intensity identifications are robust.

Advanced models (CDW, PIA, and others) predict much smaller $2p$ direct population than statistical prediction and predict peaking. Iron data [16,45] observed the same decrease of $2p$ population compared to a statistical model. Similarly, (low-n) s-state populations are predicted to be much smaller than statistical for more advanced models, as suggested by the Balmer-β spectra.

The model of M6 appears to be approximately valid for high n, and there is evidence that $4d$ populations might be reduced by 34%, $4s$ reduced by 50%, $3p$ reduced by 70%, and $2p$ reduced by 50%. Weaker evidence from Balmer α suggests that M6 may underestimate $3d$ by 50% and data about $4p$ states is ambiguous but with significant uncertainty (Lyman γ may be affected by linearization issues). Unlike the iron experiment, M5 is about as effective as M6 as a model for the germanium data. M5 suggests much more prompt decay for Lyman α and $4d$ decays from Balmer $\beta_{1,5,6}$ (Table XII). For Lyman α this only represents an error of 12 μm or 6 ppm, while for the Balmer components this is 17 μm or 8 ppm. Both shift in the same direction, hence partially cancelling contributions. Predicted corrections of low-lying states from M5 yield lower $2p$, $4s$, and $4d$ populations and hence similarly increase the downstream location of emission of these components. Hence decay locations of $n=5$ transitions and above can be reliably estimated in Table XII, column C2, by model M6, corrected in places but with relatively small uncertainty.

This methodology has been shown to work in general relativistic beam-foil spectroscopy experiments, particularly at accelerator or storage ring environments, and to provide much-needed insight into detailed theoretical predictions which we find do not explain observed data. Hence there is clear need for greater predictive capability of theoretical plasma excitation/ionization computations, especially in the accelerator and beam-foil environment. Since this has been a limiting factor in many experimental determinations, greater development would be invaluable.

XVI. SATELLITE DECAY LOCATIONS

The $2s$-$1s$ intensity is predicted to be large; 12.5%–6.5% contamination of Lyman α_2 for germanium. Mean decay

TABLE XI. Hydrogenic germanium field-free decay locations downstream of target exit plane: $\beta=0.1772$, 2 mm observation region, and 10 μg cm^{-2} target (results in micrometers).

$n'=14(l+1)-nl$	$1s$	$2p$	$3d=4d$	$4f$	$5g$	$6h$	$7i$
Decay length (in μm)	25.09	74.33	149.1	250.4	368.7	535.3	719.6

lengths are 930 μm downstream, implying a full width at half maximum on the film of 330 μm. This will double the width, reduce the peak by a factor of 2, and shift the centroid downstream of Lyman α_2 by 122.0 μm for a 2 mm observation region; for 1 mm, this shift is 39.6 μm. The M6 estimate gives a small Lyman centroid displacement of 5.7 ppm.

Balmer-β decay locations are given reliably by this discussion. Errors are naïve estimates from comparison of M6 to other models. Lyman-β locations assume in-target decay for the C1 component and dominant direct decay for C2. The intensity and location discrepancy between Lyman β and Balmer α is consistent with a p- versus d-state dependences, but the C1 component may well be due to *exit excitation* rather than in-target deexcitation, and the C1 fraction is uncertain.

Decay locations for $4f$-$2p$ depend on the Yrast contribution since convoy electrons *may* capture directly into Yrast states. This would affect Lyman α, $3d$-$2p$, $3d$-$1s$, and $4f$-$2p$ contributions [17]. Observed $4f$-$2p$ peaks will lie on the short wavelength side of the two strong $4d$-$2p$ peaks by 697.0, 328.5, and −51.1 ppm for Si diffraction. The fraction should be approximately 1.32%, 1.73%, and 0.21% for ger-

TABLE XII. Hydrogenic Ge decay locations downstream of target: 2 mm observation region, and 10 μg cm^{-2} target with results in micrometers. M0, M1, and M2 are inconsistent but are presented for completeness. C1, C2: thickness-dependent and independent components, estimated. M0: free decay length, without cascades. M1–6: models in text, including cascades (statistical, $m_l=0$, $l=0-2$, $l=n-1\rightarrow n-3$, $n^{-2/3}$, and OBK).

Line	C1	C2	M0	M1	M2	M3	M4	M5	M6
Ly δ[a]		3.8(5)	1.169	7.172	5.544	10.76	6.761	3.332	3.899
Ba ζ_{1-4}[a]		20(2)	13.69	235.3	18.23	19.99	19.25	13.74	19.99
Ly γ		3.2(5)	0.6038	0.957	5.322	10.35	5.486	2.229	3.193
Ba ζ_{5-7}		20(2)	14.13	242.8	19.33	20.47	20.55	14.18	20.47
Ba ϵ_{1-4}		16(2)	9.217	90.66	14.48	16.19	15.62	9.263	16.19
Ba ϵ_{5-7}		16(2)	9.526	94.08	15.55	16.53	16.96	9.573	16.53
Ba δ_{1-4}		13.5(5)	5.837	27.45	11.88	13.79	13.42	5.881	13.79
Ly β_1	−10.99	3.7(5)	0.258	1.494	5.584	10.35	5.446	1.362	3.724
Ly β_2	−10.99	3.7(5)	0.260	1.498	4.077	10.37	3.596	1.381	3.760
Ba δ_{5-7}		13.7(5)	6.046	28.56	12.97	14.03	14.91	6.091	14.03
Ba γ_{1-2}		13.4(5)	3.400	5.583	10.39	31.44	13.22	3.442	13.46
Ba γ_{3-4}		18.0(5)	17.80	6.801	4.121	10.81	18.04	17.97	17.98
Ba γ_{5-6}		13.6(5)	3.534	5.725	11.53	31.68	15.14	3.576	13.62
Ba γ_7		18.0(5)	17.80	25.30	19.72	18.64	18.04	17.97	17.98
$4f_{5/2}$-$2p_{1/2}$		120.6	3.626	99.50	22.16	220.2	119.6	9.576	119.2
Ba β_1		20.2(20)	1.753	9.396	10.02	53.36	18.17	1.792	18.64
Ba β_2		3.2(5)	0.6038	0.9572	5.321	10.35	5.486	2.229	3.193
Ba β_3		11.7	11.47	12.51	3.871	12.42	11.74	11.64	11.65
Ba β_4		3.2(5)	0.6056	0.9561	13.60	10.37	3.597	2.252	3.217
Ly α_1	−11.17	27.1(20)	0.0779	11.60	6.230	82.73	15.87	0.703	13.32
Ly α_2	−11.17	27.1(20)	0.0790	11.71	4.642	83.05	10.48	0.719	13.53
$2s$-$1s$ rM1	−11.17	930	4683	929.1	930.7	930.3	929.3	929.1	929.2
$4f_{7/2}$-$2p_{3/2}$		120.6	3.685	99.62	23.54	220.4	131.4	9.808	119.3
$4f_{5/2}$-$2p_{3/2}$		120.6	3.626	99.50	22.16	220.2	119.6	9.576	119.2
Ba β_5		20.3(20)	1.833	9.490	11.27	53.52	21.54	1.872	18.74
Ba β_6		20.2(20)	1.753	9.396	10.02	53.36	18.17	1.792	18.64
Ba β_7		11.7	11.47	12.51	13.60	12.42	11.74	11.64	11.65
Ba α	−10.47	60(2)	0.7841	43.15	12.57	157.2	62.32	0.8167	54.60

[a]Tabulated decay lengths are for the dominant multiplet component.

TABLE XIII. Scaling for the germanium experiment (μm) and effect of experimental uncertainty on the Lyman-α–Balmer-β region for Si 111 diffraction, $2R_z=300$ mm at $\lambda=4.755\,427$ Å/(1–4), π and σ polarizations.

Scaling: $\frac{\Delta\lambda/\lambda}{\Delta Y_{iz}}=2.915$; 2.793 ppm/$\mu$m (Ba β_{1-4}; Balmer β_{5-7}); $\frac{\Delta f_{Lamb}}{\Delta\lambda/\lambda}=\Delta E/E_{Lamb}/\frac{\Delta\lambda}{\lambda}=1.319\,95\times10^{-3}$/ppm							
Order, polarization		1st, σ	1st, π	4th, σ	4th, π	4th-1st, σ	π
Spectrometer parameters: $w_0=0(2)$ mm, $w=\pm5$mm$\rightarrow\alpha_1=0\pm.0184^R$	(film height)	−0.29	−0.28	−0.89	−0.55	−0.60(30)	−0.27(30)
$\beta=0.1772(3)$, $f_{Lamb}=0\pm1$, $\alpha_{Bm}=0.00(2)$?, effect via $\frac{\Delta\lambda}{\lambda}$ 0 ± 0.0025?	(α_{Bm}, expt.)	+0.57	+1.43	+1.11	+1.11	+0.54(30)	−0.32(30)

manium (model M6 neglecting additional pure Yrast decays). These values will lead to small possible 9.2, 5.7, and −0.11 ppm shifts for germanium. Values for Lyman α follow from corrected M6 values, with largest uncertainties from the Yrast contribution, the possibility that the C1 fraction may be overestimated, and the relatively large uncertainty in the C1 decay location.

XVII. LAMB SHIFT IN HYDROGENIC GERMANIUM

We are now in a position to provide detailed estimates on contributions to the final Lamb shift measurement and error analysis. Table XIII summarizes some of the key scalings between units in the Lyman-α–Balmer-β spectral region. Experimental uncertainty of velocity is not significant. Table XIV summarizes contributions from the local fits, from refractive index shifts (corrected from earlier estimates), satellites, and other sources. Comparison is made to the values used in the original analysis [15] to demonstrate part of the quantitative improvement made. Dominant uncertainties, neglecting curved crystal effects, were noted as due to centroid location in the diffraction profile and to Lorentzian versus Gaussian fitting of the data. The earlier analysis did not use the current linearization procedure, leading to a larger quoted uncertainty, and did not use Lorentzian profiles convolved with slit or Gaussian (Voigt) profiles also yielding a larger uncertainty estimate. Correction of earlier data for effects listed here uses our current diffraction, densitometry, and polarization estimates but must include large 35/27 ppm uncertainties for fitting simple functions to an unknown profile (due to discrepancy between Lorentzian and Gaussian fitted results).

There is an apparent anomalous fine structure splitting in BX25A (much less significant for the other data), so global fits incorporating both components yield different results depending on the reference line used to define the zero position. Fits have been obtained using Lyman α_1, Lyman α_2, and Balmer β_5 ("$4d_{5/2}$-$2p_{3/2}$") as reference lines (not tabulated). In these three procedures, dispersion variables α', BDz, BXz, and w_0 vary insignificantly (see [17] for definitions of minor variables), and $\beta=v/c=0.176\,96$, 0.176 80, and 0.177 07, respectively, well within quoted fitting uncertainty of 0.0035 and in agreement with measured velocity 0.1772 ± 0.0003, contributing potential diffraction corrections of less than 0.1 ± 0.1 μm. α_{Bm} lies between 2.8×10^{-4R} and 8.7×10^{-5R}, which is better than estimated uncertainty of 2×10^{-2R}. Minor parameters α'' and $Ns_{\rm scale}$ vary but remain within physical limits and do not contribute significant shifts. The crystal curvature on the axis of the generatrix, $2Rz$, varies from 299.805 to 299.855 mm compared to estimated uncertainty of $300.0\pm.1$ mm. If due to crystal rather than Rowland circle effects, this could give shifts of $+0.37\pm0.59$ μm or 1 ppm, with the variation between fits at 25% of these values. These results are consistent for BX22A, with $2Rz$ varying from 299.863 to 299.848 mm, $\beta=v/c$ from 0.17689 to 0.17674, and α_{Bm} larger but still only -0.0021^R to -0.0026^R. All these results are broadly consistent.

However, unsurprisingly, the extrapolated Lamb shift parameter $f_{\rm Lamb}$ varies for BX25A from $-0.086\,95\pm0.005\,44$ to $-0.116\,44\pm0.0050$ and $-0.107\,81\pm0.002\,78$, and for BX22A from $-0.080\,43\pm0.0137$ to $-0.111\,99\pm0.0109$ and $-0.098\,29\pm0.0084$, as indicated in the table. Using Lyman α_2 as the reference line includes significant satellite ($2s$-$1s$) effects should therefore be rejected and gives a partial explanation of the cause of the discrepancy. Use of Lyman α_1 gives the global shift dominated by the Lyman-α_1 versus mean Balmer-β value, while that using Balmer β_5 gives a result based on the (weighted) mean of all Lyman peaks, compared to Balmer β_5. The dispersion is correct in both cases.

Statistical uncertainty has been reduced by factors between 2 and 7 compared to earlier results due to improvements in analysis. Results for global fits show further potential reduction. Scatter between films is also much lower, but mean results for the two (best) data sets are consistent. Trends with thickness are clearer and more reliable. Diffraction corrections are necessary and improved analysis is important, but additional investigation remains indicated. Inclusion of $2s$-$1s$ contributions for a 2 mm observation region improve the fine structure separation dramatically and in fact almost exactly remove the anomaly between Lyman α_1 and Lyman α_2. Lyman γ can be seen on several scans and is well resolved from Lyman α_2 (as claimed), so gives negligible shifts of results. Dielectronic $2s$-$1s$ and $4f$-$2p$ satellite contaminations are much more significant for this germanium experiment compared to iron.

TABLE XIV. Hydrogenic germanium Si 111 measurements and corrections: shifts in ppm from theory with uncertainties. idem: same as previous column.

Film emulsion	BX25A	XG25L	BX22A	XG22U	[6,15]	[6,15]
C target[a]	10	10	50	50	10	50
$h(f)$ (mm)	0.40	1.00	0.40	1.00	1.00	1.00
Useful scans[b]	21-5	6	15-2	6		
Mean result of local (Ly α–Ba β) fits with scatter: shifts in ppm from theory						
Lyman α_1	$+65.9 \pm 4.1$	-93.2 ± 9.4	$+75.5 \pm 4.9$	-35.8 ± 35		
Lyman α_2	$+92.8 \pm 3.2$	-75.2 ± 12	$+98.7 \pm 5.3$	-26.6 ± 19		
Result of weighted global fits of Lyman-Balmer series for all scans, including above (ppm)						
Ref=Lyman α_1	$+65.9 \pm 4.1$		$-+60.9 \pm 10.4$			
Ref=Balmer β_5	$+81.7 \pm 2.1$		$+74.5 \pm 6.4$			
Total additional offset from diffraction computations, Table VII (ppm)						
Lyman α_1	-23.04 ± 9.2	$+97.07 \pm 36.2$	-23.04 ± 9.2	$+97.07 \pm 36.2$		
Lyman α_2	-22.79 ± 9.1	$+94.71 \pm 28.5$	-22.79 ± 9.1	$+94.71 \pm 28.5$		
Corrected mean results of local (Ly α–Ba β) fits (ppm)						
Lyman α_1[a]	$+42.86 \pm 4.1$	$+3.87 \pm 9.4$	$+52.46 \pm 4.9$	$+61.27 \pm 35$		
Lyman α_2[a]	$+70.01 \pm 3.2$	$+19.51 \pm 12$	$+75.91 \pm 5.3$	$+68.11 \pm 19$		
Dielectronic satellites, corrections to above (ppm)						
Lyman α_1	-0.972 ± 1.02	Idem	-4.86 ± 5.1	Idem	-4	-20
Lyman α_2	-1.946 ± 2.01	Idem	-9.73 ± 10.0	Idem	-4	-20
$2s$-$1s$, Ly α_2	-17.56 ± 5.0ppm	Idem	Idem	Idem		
$4f$-$2p$ decays, Ly α_1	-8.18 ± 5.0	Idem	Idem	Idem		
Ly α_2	-7.24 ± 4.0	Idem	Idem	Idem		
Fitting error, Ly α_1	-2.70 ± 3.75	Idem	Idem	Idem	Discussed	
Lyman α_2	-1.26 ± 4.58	Idem	Idem	Idem	Discussed	
Stark effects, Ly α_2	-3.45 ± 3.45	Idem	-8.98 ± 8.98	Idem	Idem	Idem
C2 decay source, Ly α_1	-7.00 ± 7	Idem	Idem	Idem		
Ly α_2	-6.92 ± 7	Idem	Idem	Idem		
Yrast shift/2 mm	-39.40 ± 14	Idem	Idem	Idem		
Results (ppm)						
Total, Ly α_1[c]	24.01 ± 4.1	-14.98 ± 9.4	29.72 ± 4.9	38.53 ± 35		
Ly α_2[c]	31.63 ± 3.2	-18.87 ± 19.5	24.22 ± 5.3	16.42 ± 19		
Uncertainty, Ly $\alpha_{1,2}$	$\pm 13.8, 14.8$	$\pm 38.6, 32.9$	$\pm 14.9, 20.1$	$\pm 51.5, 38.3$		
Yrast limit, Ly $\alpha_{1,2}$	$-8.39, -0.85$	$-47.4, -51.4$	$-2.68, -8.26$	$6.13, -16.06$		

[a]Target thickness (μg cm^{-2}).
[b]See text.
[c]Statistical uncertainty only.

Possible shifts and uncertainties attributed to a Balmer fitting error are reduced by a factor of 2–3 (compared to the iron measurement), and the intensity uncertainty due to statistics is small at the 1%–2% level. This corresponds to possible Balmer β_1 shifts to lower wavelength (as for iron) by 4.27 ± 4.27 ppm, and Balmer β_5 shifts to longer wavelengths (opposite to iron) by 1.27 ± 7.64 ppm, giving the tabulated correction.

Stark effects have been discussed in detail by Laming [6,15,47]. Calculation was based on intensity ratios for Lyman α and β, and on estimated 2×10^9 V/cm wake fields inside the target. Authors concluded that additional shifts of $+15 \pm 15$ ppm for Lyman α_2 and of $+23 \pm 23$ ppm for Lyman β_2 were possible for excited n=2-3 levels produced inside the target. Speculation concerning n=4 levels concluded that the effect was not likely to dominate, though if all n=4 decays took place inside the foil additional −220 ppm shifts may be involved. We have shown herein that Balmer radiation is neither excited nor emitted inside the foil since capture occurs at the exit. This agrees with the conclusion based on decay lengths and width discrepancies. Stark effects due to component mixing on intensity ratios (for Balmer levels)

have been discussed. Quoted shifts for weak Lyman components must also be scaled by the C1 component fraction, which has now been estimated at 22% for Lyman α and 11% for Lyman β (10 μg cm^{-2} targets). Resulting shifts are given in the table.

The other Stark effect discussed by Laming relates to nonstatistical Lyman-β and Lyman-α component ratios. The author's conclusions regarding Lyman β have been confirmed by correct linearization and improved fitting procedures, showing that Lyman β_1 is stronger than expected from standard capture models and that this discrepancy increases strongly with thickness, so is (primarily) due to the C1 component. The proposed Stark capture model suggested that Lyman β_1 (i.e., the $2_{3/2}$-$1s_{1/2}$ component) could dominate by factors of up to 3.9:1 for germanium and 5.9–6.2:1 for iron. This is strongly model dependent but is qualitatively in good agreement with observations.

The C2 component shift gives a much smaller (6.9 μm) downstream shift compared to iron measurements, with the discussion of population models increasing the Lyman-α decay length by 25% and hence the overall estimate by a further 6.8 μm. The Yrast limit corresponds to a smaller correction because of the lower 40% maximum component estimated from relative intensities and due to the Z^3/β scaling. The mean location for the Yrast component is approximately 203 μm neglecting $n=4$ states or 119 μm including them. The larger estimate gives a mean location downstream of 97.46 μm for Lyman-α radiation (again neglecting the C1 decay pattern) or a 13.68 μm shift along the film compared to Balmer β.

Comparisons of profile widths are in good agreement with the earlier discussion. Thickness-dependent corrections are at least approximately correct. All estimates (except for the Yrast limit) were made prior to the summation of results, which has no effect on the arguments used to derive them but helps to rule out deliberate or accidental random correction factors.

Results give Lyman-$\alpha_{1,2}$ discrepancies of $24.01 \pm 4.1 \pm 13.2$ and $31.63 \pm 3.2 \pm 14.5$ ppm for BX25A, with $29.72 \pm 4.9 \pm 14.1$ and $24.22 \pm 5.3 \pm 19.4$ ppm for the thicker target and BX22A. These estimates are in good agreement, and note that the thinner targets might be expected to be more accurate because of the minimization of the C2 component and the C2 correction.

Correction of earlier results for effects outlined above (XG25L and XG22U) involves the dominant Lorentzian profile fitting uncertainty of 35–27 ppm. Scatter in the earlier data is large, and for the thicker targets becomes dominated by fitting errors, statistics, and thickness-dependent components to contribute little to any final conclusion. Final uncertainties for earlier analysis are rough estimates, and the summation in Table 3.17 of [6] gained a minimum statistical uncertainty of 4.6 ppm from 67 scans, but without correction for thickness-dependent effects. Despite these uncertainties, results are in generally good agreement with one another. The current most reliable result is provided by the weighted mean of the results for BX25A and BX22A. This is presented in Table XV. Also summarized in Table XVI are the results of the earlier analysis for comparison.

The second estimate provided in Table XIV is the lower (Yrast) limit assuming Yrast population of $n>4$, $l>3$ states (and mainly $l=n-1$) primarily affecting $2p$-$1s$, $3d$-$1s$, $3d$-$2p$, and $4f$-$2p$ transitions. This population mechanism would yield equal Lyman-α and Balmer-α intensities with Lyman β at the 1% level and $4f$-$2d$ transitions at the 0.5% level, arising from the same source location. This could account for 40% of the Lyman α intensity, constrained by widths and relative intensities [16].

TABLE XV. Hydrogenic germanium Si 111 means of results from Table XIV: shifts in ppm from theory with uncertainties.

Results (ppm)	BX	XG
Total, Ly α_1[a]	26.36 ± 2.8	-4.40 ± 12
Ly α_2[a]	29.65 ± 3.3	-12.94 ± 12
Uncertainty, Ly $\alpha_{1,2}$	$\pm 13.5, 14.9$	$\pm 39.3, 32.9$
Yrast limit, Ly $\alpha_{1,2}$	$-8.39, -8.26$	

[a]Statistical uncertainty.

Uncertainty of downstream decay lengths is still large but is much reduced due to the germanium excitation and capture conditions and gives a smaller uncertainty (7 ppm) than diffraction crystal thickness and angular tolerances (9.2 ppm). The dominant additional uncertainty is the Yrast contribution, but here this limit is somewhat better defined by the data (Table XIV). For this germanium experiment, uncertainties for dielectronic satellites rapidly dominate with modest increases of thickness from 2 ppm (thin foil) to 10 ppm (thicker foil). Similarly, possible Stark effects become dominant (9 ppm) for thick foils but are modest for thin foils (3.5 ppm). $2s$-$1s$ satellite contamination (which is real and implicitly observed in the data) only affect Lyman α_2 but has an uncertainty of 5 ppm, so remains significant at the level of accuracy reported, and the often-neglected $4f$-$2p$ decays have estimated significant uncertainties of 4–5 ppm Compared to these uncertainties, statistical imprecision is only 2.8 or 3.3 ppm and other uncertainties are negligible.

Table XV yields 13.5 and 14.9 ppm measurements of Lyman-α wavelengths with $+3.5 \pm 1.8\%$ and $+3.9 \pm 2.0\%$ measurements of Lamb shift contributions to these intervals. This measurement is reasonably consistent with theory at the two standard deviation level, as opposed to earlier work which omitted significant systematics. The accuracy is improved by a factor of 2.8 compared to earlier work. This measurement is significantly more accurate than a result from an iron experiment by the same authors [17], in part because of the increase in significance of QED with atomic number and the improved diffraction crystal, statistics, and lower uncertainty relating to Yrast cascade populations.

XVIII. HYDROGENIC GERMANIUM $2P_{3/2}$-$2P_{1/2}$ FINE STRUCTURE

Many of the dominant uncertainties are systematic and are consistent for Lyman-α_1 and Lyman-α_2 components. Hence the uncertainties in the measurement of the difference—i.e., the fine structure interval—will cancel to first order. This is summarized in Table XVII. The statistical uncertainty of a differential measurement is necessarily larger [by about $\sqrt{(2)}$

TABLE XVI. Differential measurement of germanium Lyman α wavelengths and $2p$-$1s$ Lamb shifts.

	Lyman α_1	Lyman α_2
Local discrepancy (ppm)[a]	26.4[2.8][13.2]	29.7[3.3][14.5]
[15] 10 μg cm^{-2} target (ppm)[b]	−69.4[13.7]	−62.1[12.8]
[6] final result (ppm)	−87[38]	−83[30]
Wavelengths (Å)	1.1669938[33][169]	1.1724336[39][170]
Theory [29] (Å)	1.1669630[8]	1.1723988[8]
Theory [30] (Å)	1.1669894[143]	1.1724248[150]
Lamb shift (cm^{-1})	66080[237][1121]	67169[281][1237]
Theory [29] (cm^{-1})	63842[63]	64640[60]

[a]Statistical followed by systematic uncertainty. ppm relates to [29].
[b]q.v. text.

or 4.2 ppm] and the systematic uncertainties are reduced to a total of 6 ppm Diffraction shifts, source location shifts, and fitting shifts affect both equally and therefore cancel to first order. Only $2s$-$1s$, Stark and dielectronic satellite uncertainties, and small uncertainties from asymmetric Balmer shifts contribute to uncertainty of the fine-structure separation. Therefore, it is possible to get high accuracy on a differential measurement of the fine structure separation based on this same data set.

The results provide an interesting fine-structure measurement. In this case relatively large thickness-dependent and $2s$-$1s$ corrections do not cancel, and the two measurements are in less close agreement. The direct unweighted sum of individual scans (corrected for differential target thickness effects) again improves consistency and avoids double counting of error contributions. Hence this is a particularly valuable test of the first-order fine structure Lamb shift in a new environment, and a confirmation at this level of theory.

TABLE XVII. Germanium $2p_{1/2}$-$2p_{1/2}$ fine structure.

Target thickness (μg cm^{-2})	10	50	Mean
Correction (ppm of wavelength)			
From Table XIV[a]	7.62 ± 5.2 ppm	-5.50 ± 7.2 ppm	3.12 ± 6.2 ppm
From individual scans[b]	$+26.85 \pm 4.15$ ppm	$+17.87 \pm 3.72$ ppm	$+23.16 \pm 2.95$ ppm
Diffraction uncertainty	± 0.86 ppm		
Dielectronic satellites[c]	-0.974 ± 2.24 ppm	± 11.2 ppm	
$2s$-$1s$+Ly ξ	-17.56 ± 5.0 ppm		
$4f$-$2p$ decays	$+.94 \pm 0.6$ ppm		
Fitting error	$+1.44 \pm 2.28$ ppm		
Stark effects[c]	-3.45 ± 3.45 ppm	± 8.98 ppm	
Decay source	$+0.08 \pm 0.4$ ppm		
Total (ppm of wavelength)[a]	$7.62 \pm 5.2 \pm 7.0$ ppm	$-5.50 \pm 7.2 \pm 15.4$ ppm	$3.12 \pm 6.2 \pm 7.0$ ppm
[15] 10 μg cm^{-2} target	7.3 ± 14 ppm		
[6] final result (ppm)	4 ± 38		
Total (ppm of wavelength)[b]	$7.33 \pm 4.15 \pm 6.0$ ppm	$-1.65 \pm 3.72 \pm 15.4$ ppm	$3.63 \pm 2.95 \pm 6.0$ ppm
Total (ppm of f.s. interval)[b]	$+1574 \pm 891 \pm 1288$	$-354 \pm 799 \pm 3306$	$+779 \pm 633 \pm 1288$
Δ (cm^{-1}) experiment−theory	$+625 \pm 354 \pm 512$	$-141 \pm 317 \pm 1313$	$+309 \pm 251 \pm 512$
Experiment, this work	$397617 \pm 251 \pm 512$ cm^{-1}		
Theory [29]	397308 ± 3 cm^{-1} = ± 7.6ppm f.s.		
Lamb shift contribution [29]	798 ± 2.3 cm^{-1} = 2009 ± 5.8ppm f.s.		
Theory [30]	397260 ± 103 cm^{-1} = ± 259ppm f.s.		

[a]Correlated errors summed in quadrature (i.e., overestimated).
[b]Direct sum over individual scans excluding most (e.g., $2s$-$1s$) systematic corrections, but including 50 vs 10 μg cm^{-2} thickness-dependent corrections.
[c]The number in brackets refers to the thicker target uncertainty.

TABLE XVIII. Germanium heliumlike $1s2p\ ^1P_1$-$1s^2$ and $1s2p\ ^3P_1$-$1s^2$ wavelengths; ppm discrepancies from theory of Drake [32].

	Theory (Å)		Experiment		
Line	[32]	[33]	This work	Discrepancy	[78]
$1s2p\ ^1P_1$-$1s^2$	1.206056(2)[a]	1.206137(1200)	1.206030(17)	-22.0 ± 14.3 ppm	1.205990(26)
$1s2p\ ^3P_1$-$1s^2$	1.213066(2)[b]	1.213022(1200)	1.213042(27)	-20.0 ± 22.5ppm	1.212940(41)

[a]Alternate theory: 1.206 050 [79]; 1.206 027 [80]; and 1.206 043 [82].
[b]Alternate theory: 1.213 063 [79]; 1.213 037 [80].

The result gives a 1435 ppm measurement of the fine-structure interval, or 71% of the QED contribution to the fine structure interval, with the statistical level at the 31% level but dominated by systematic uncertainties. This is an improvement by a factor of almost 6 compared to the earlier analysis. The result is only 0.5σ (standard deviations) discrepant from theory.

XIX. SECONDARY FEW-ELECTRON GERMANIUM LINES

Decay modeling suggests that Lyman β will be produced approximately 23 μm upstream of Lyman α or approximately 17 μm upstream of Balmer β_5. Relatively weak experimental data suggests that Lyman β does indeed lie above the dispersion relation as this would imply (by approximately 40 ± 20 μm). The main overall correction of downstream location is smaller than before (30 μm upstream or 15.2 ppm) and the larger Stark effect (perhaps up to $+23 \pm 23$ ppm for Lyman β_2) will counteract this for the weak component with $3d$-$1s$ possibly giving a shift of similar size, and no shift from ns-$1s$ transitions. The dominant effects may then be diffraction and fitting shifts. The final result is then consistent with theory to within 20 ppm, but with a relatively large uncertainty of approximately 31 ppm.

Secondary peak locations may be used to measure wavelengths of secondary peaks, and $1s2p$ populations are observed in third- and fourth-order diffractions. These transitions are generally produced by multiple interaction in target. As thicknesses increase, so satellite contamination rapidly becomes significant. Also, third order results have significant systematics due to fourth-order Lyman-δ overlap and linearization uncertainty. Hence we report the thin target results using fourth order diffraction in Table XVIII, which also obtained the lowest statistical uncertainty. Precision is improved compared to [17] because source corrections are smaller. $1s2p$-$1s^2$ wavelengths are well defined. Uncertainty tabulated refers to statistical scatter. Theory quoted is that of Drake [32]. $1s3p$-$1s^2$ was observed in Si(Li) spectra but was not fitted in the photographic data (statistical uncertainties were larger). Systematics vary with the dispersion relation, and radiation in fourth order is consistent (avoiding Lyman-δ contamination in third order). This result yields wavelengths slightly lower than Drake, which might be affected by the in-target production and decay. Despite the limitations from statistics and systematics, this provides a more accurate and consistent result than [78] and confirms modern theory compared to earlier computations. Determinations of the (strong) w transition have been made before in this region of Z—this is one of the most accurate. All-orders, configuration interaction (CI), and multi—configuration Dirac-Fock computations have been made for these transitions [79–81]. Interestingly, greatest agreement lies with the first CI computations using the latter correction [80], rather than the more recent correction of that work [82]. It would be foolish to discriminate too much with the current data, as the unified, all-order, and CI treatments are all in fairly good agreement with the data within uncertainty.

It is interesting to note strong evidence for the excitation conditions affecting the helium-like spectra. For example, electron-beam ion-trap sources appear to be able to be tuned to observe $1s2p\ ^1P_1$, $^3P_2$, $^3P_1$ and $1s2s\ ^3S_1$ transitions (w,x,y,z) while in-target collision seems to produce (w,x,y) [83–85].

Perhaps more importantly, these heliumlike resonance transitions provide a fine structure measurement of $479\,318 \pm 1186 \pm 1852$ cm^{-1} with statistical uncertainty from $1s2p\ ^1P_1$ and $^3P_1$, respectively, in good agreement with the theory of Drake [32] ($479\,144 \pm 240$ cm^{-1}), Cheng [80], and Plante [79] below the 0.5σ level, but in significant disagreement with the earlier theory of Vainshtein [33] ($470\,600 \pm 8290$ cm^{-1}). Hence this measurement critically tests heliumlike theory and unexpectedly suggests tantalising possible agreement with the latter correction.

XX. SUMMARY AND CONCLUSION

This study provides precise wavelengths for Lyman α in hydrogenic germanium of $1.166\,993\,8 \pm 33 \pm 169$ and $1.172\,433\,6 \pm 39 \pm 170$ Å. This represents improvement by a factor of 3 with respect to earlier analysis and estimates, both with respect to the uncertainty and the discrepancy from theory. As opposed to earlier work, the sign of the discrepancy is the same for iron and germanium results, corresponding to a shift to longer wavelengths. Dominant systematics are due to diffraction parameters including crystal thickness and alignment, differential Doppler shifts due to the variable location of spectral emission downstream of the beam-foil target, and dielectronic $2s$-$1s$ and $4f$-$2p$ satellites.

The result is one of the most accurate tests of QED in medium-Z hydrogenic systems and is in good agreement with the earlier theory of Erickson [30], and that of Mohr

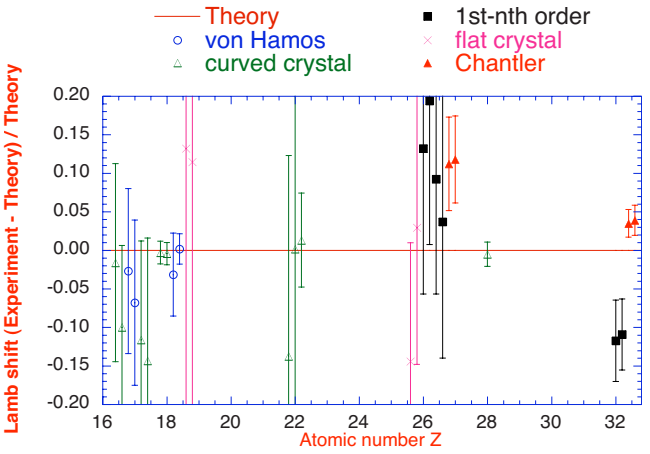

FIG. 11. (Color online) Comparison of experiment for the $1s$-$2p$ Lamb shift to theory, relative to Mohr [28]. Points are marked according to the detection methods used. In general, Von Hamos geometries have higher flux and statistics but more complex problems regarding calibration; and flat crystal measurements can have very high resolution, relatively low flux, but are extremely sensitive to small systematics regarding calibration and alignment. Results are paired with Lyman α_1 ($1s$-$2p_{3/2}$) followed by Lyman α_2 ($1s$-$2p_{1/2}$) where reported. In order of Z, references are $Z=17$: [86–88]; $Z=18$: [89,90,84]; $Z=22$: [91,92]; $Z=26$: [10,17,93,94]; $Z=28$: [95]; and $Z=32$: [6], this work.

[28] and Johnson and Soff [29]. In this sense we are primarily testing the self-energy and vacuum polarization and are more pointing the way toward future developments where a modest improvement could discriminate multiple virtual photon terms. Future measurement of systematics with an uncertainty improved by a factor of 2 will provide a particularly stringent test of these theories.

Figure 11 shows the accuracy obtained in this measurement, compared to earlier measurements using a variety of techniques in the intermediate Z range. Details of experimental configurations and potential systematics have been discussed recently [97]. However, note that (i) fine-structure measurements require the collection of x-ray data for both Lyman components; (ii) the dispersion plane should ideally obtain similar discrepancies for both components if the cause is the $1s$ Lamb shift; (iii) several of the systematics involved have not been calculated in earlier analyses; and (iv) no depth penetration computations have been made yet for the von Hamos geometry.

All measurement involving crystal diffraction should include depth penetration corrections for expected shifts. For flat crystals these are an order of magnitude smaller than for the curved crystal radii of this thesis, but this may still typically correspond to a 10 ppm correction. The correction increases with curvature and transition energy and decreases with the mean atomic number of the scattering units.

Results extracted for the $2p_{3/2}$-$1s_{1/2}$ and $2p_{1/2}$-$1s_{1/2}$ Lamb shifts are $66\,080 \pm 237 \pm 1121$ and $67\,169 \pm 281 \pm 1237$ cm^{-1} compared to theoretical estimates of $63\,842 \pm 63$ and $64\,640 \pm 60$ cm^{-1}, respectively. This 14 ppm measurement of the wavelengths thus provides 1.8% and 2.0% measurements of the $2p$-$1s$ Lamb shifts.

A precise measurement of the $2p_{3/2}$-$2p_{1/2}$ fine structure is obtained. Due to the limited data set, statistical imprecision from fitting error uncertainty and from centroid location uncertainty are larger, and the higher Z leads to larger corrections from satellites and particularly $2s$-$1s$ transitions. Stark effects and uncertainty may be overestimated. This result is not so accurate as a test of the QED contribution to fine structure as a recent measurement in hydrogenic iron [17] but is much more accurate than the earlier best quoted measurement in the region (also for hydrogenic iron [96]).

The results indicate agreement with both theoretical calculations at the 0.5σ level. The discrepancy obtained compared to the theoretical separation of $397\,308 \pm 3$ cm^{-1} is $+309 \pm 251 \pm 512$ cm^{-1}. $2s$-$2p$ Lamb shift measurements at the 1% level in argon, at the 0.2% level in sulfur, and at the 25 ppm level in helium are sensitive to $2p$ QED at the 36%, 7%, and 0.2% levels [116–118] but do not observe $2p$ fine-structure intervals, so may be dominated by corresponding $2s$ shifts. The current 0.14% fine-structure precision result gives a critical $2p_{3/2}$-$2p_{1/2}$ fine-structure measurement above $Z=2$ sensitive to the corresponding Lamb shift contribution (at the 70% level).

The fine-structure separation for heliumlike $1s2p\ ^3P_1$-$1s^2$ to $1s2p\ ^1P_1$-$1s^2$ has been measured for germanium dominated by statistics. Corresponding fine structure measurement in heliumlike systems appears to be sensitive to or approaching sensitivity to $2p$ state QED contributions in $1s2p$ systems [12,77,98–103], subject to possible $1s$ or $2s$ contribution errors and electron correlation uncertainties, and after correction for significant contributions [104–107]. Some of these issues and advances have been discussed recently [108,109]. Direct measurement of heliumlike $1s2p\ ^3P_1$-$1s2p\ ^3P_2$ by laser-induced M6 resonance has quoted a measurement of the fine-structure interval of fluorine at the 22 ppm [110,111] or 32 ppm [112–114] level, of very high accuracy, but disagreed with theory by 30σ. Conversely, the agreement of the current result with theory is very good. In low Z regimes, good success has also been observed for laser resonance experiments [115]. The present accuracy is high compared to other heliumlike measurements in this range of Z [77].

Most of the literature observes fine-structure separations consistent with neglect of $2s$-$1s$ contributions. The $2s$-$1s$ correction depends on the observation length involved and on the detection method, which will be different in different spectrometer arrangements, but the effect is quite clear in these data. Dominant uncertainty in the Lamb shift measurement remains the Yrast contribution, initial populations, and observation region, with possible fitting errors, diffraction corrections, and statistics contributing in order of decreasing significance. Neither crystal defects nor photographic linearization were significant limitations of the accuracy, and in general the statistics were excellent. However, this did require careful evaluation of photographic theory [25–27].

This work depended on in-beam calibration lines. At an accelerator facility this (Lyman-α–Balmer-β) approach automatically cancels several effects relating to Doppler shifts. We note that secondary cancellations were also necessary, including the use of paired Johann circles on opposite sides of the beam and using two-dimensional detection to quantify the slope of the image. The simultaneous measurement of the Lyman and Balmer series permitted calibration of the disper-

sion of the crystal spectrometer to high accuracy, beyond the Lyman-α–Balmer-β intercomparison technique and permitted an extensive analysis of the population mechanisms in a beam-foil environment.

We have assessed contributions of dielectronic satellites, Lyman-γ, $2s$-$1s$, and $4f$-$2p$ components which have generally been neglected in earlier analyses. We find that their contributions are small compared to the statistical precision, the dynamical diffraction theoretical uncertainty for this experiment, and the fitting errors. We have considered limits to the final results based on profile widths, model analysis, and Yrast limits and find that each method yields a consistent result.

The parametrized methodology for testing beam-foil interactions provide much-needed insight into detailed theoretical predictions which we find do not explain observed data. Greater predictive capability of theoretical plasma interactions are required, especially in accelerator and beam-foil environment. This limiting understanding has been a factor in many experimental determinations.

The 2σ (standard deviation) discrepancy from theory could possibly relate to dominant uncertainties from Yrast contributions, initial populations, and decay locations in the observation region. However, the result compares well with past measurements in this region of Z. The key problem relates to the Doppler shift arising from differences in the source location. Even with a 1 or 2 mm observation length this remains a dominant limitation of this particular experiment.

[1] H.-D. Betz, Rev. Mod. Phys. **44**, 465 (1972).
[2] A. B. Wittkower and H.-D. Betz, At. Data **5**, 113 (1973).
[3] K. Shima and T. Mikumo, At. Data Nucl. Data Tables **34**, 357 (1986).
[4] S. J. Brodsky and P. J. Mohr, in *Structure and Collisions of Ions and Atoms*, edited by I. A. Sellin (Springer-Verlag, Berlin, 1978), pp. 3–67.
[5] A. F. McClelland, J. S. Brown, B. P. Duval, E. C. Finch, H. A. Klein, J. Laursen, D. Lecler, P. H. Mokler, and J. D. Silver, Nucl. Instrum. Methods Phys. Res. B **9**, 706 (1985).
[6] J. M. Laming, C. T. Chantler, J. D. Silver, D. D. Dietrich, E. C. Finch, P. H. Mokler, and S. D. Rosner, Nucl. Instrum. Methods Phys. Res. B **31**, 21 (1988).
[7] M. Niering *et al.*, Phys. Rev. Lett. **84**, 5496 (2000).
[8] P. J. Mohr and B. N. Taylor, Rev. Mod. Phys. **72**, 351 (2000).
[9] G. W. F. Drake, W. Nortershauser, and Z.-C. Yan, Can. J. Phys. **83**, 311 (2005).
[10] J. D. Silver, A. F. McClelland, J. M. Laming, S. D. Rosner, G. C. Chandler, D. D. Dietrich, and P. O. Egan, Phys. Rev. A **36**, 1515 (1987).
[11] S. B. Utter, P. Beiersdorfer, and G. V. Brown, Phys. Rev. A **61**, 030503 (2000).
[12] C. T. Chantler, D. Paterson, L. T. Hudson, F. G. Serpa, J. D. Gillaspy, and E. Takacs, Phys. Rev. A **62**, 042501 (2000).
[13] S. G. Karshenboim, Phys. Rep. **422**, 1 (2005).
[14] U. D. Jentschura and J. Evers, Can. J. Phys. **83**. 375 (2005).
[15] J. M. Laming, Ph.D. thesis, Oxford University (1988).
[16] C. T. Chantler, Can. J. Phys. **86**, 331 (2008).
[17] C. T. Chantler, J. M. Laming, D. D. Dietrich, W. A. Hallett, R. McDonald, and J. D. Silver, Phys. Rev. A **76**, 042116 (2007).
[18] P. Beiersdorfer, Nucl. Instrum. Methods Phys. Res. B **56-57**, 1144 (1991).
[19] C. J. Hailey *et al.*, J. Phys. B **18**, 1443 (1985).
[20] D. D. Dietrich, G. A. Chandler, R. J. Fortner, C. J. Hailey, and R. E. Stewart, Phys. Rev. Lett. **54**, 1008 (1985).
[21] D. D. Dietrich *et al.*, Nucl. Instrum. Methods Phys. Res. B **9**, 686 (1985).
[22] C. T. Chantler, Ph.D. thesis, Oxford University, (1990).
[23] V. I. Kushnir, J. P. Quintana, and P. Georgopoulos, Nucl. Instrum. Methods Phys. Res. A **328**, 588 (1993).
[24] A. J. Varney, Ph.D. thesis, Oxford University, (1995).
[25] C. T. Chantler, Appl. Opt. **32**, 2371 (1993).
[26] C. T. Chantler, Appl. Opt. **32**, 2398 (1993).
[27] C. T. Chantler, J. D. Silver, and D. D. Dietrich, Appl. Opt. **32**, 2411 (1993).
[28] P. J. Mohr, At. Data Nucl. Data Tables **29**, 453 (1983).
[29] W. R. Johnson and G. Soff, At. Data Nucl. Data Tables **33**, 405 (1985).
[30] G. W. Erickson, J. Phys. Chem. Ref. Data **6**, 831 (1977).
[31] S. Klarsfeld and A. Maquet, Phys. Lett. **43B**, 201 (1973).
[32] G. W. F. Drake, Can. J. Phys. **66**, 586 (1988).
[33] L. A. Vainshtein and U. I. Safranova, Phys. Scr. **31**, 519 (1985).
[34] L. C. Northcliffe and R. F. Schilling, Nucl. Data, Sect. A **7**, 233 (1970).
[35] J. F. Ziegler, *Handbook of Stopping Cross-Sections for Energetic Ions in All Elements*, The Stopping and Ranges of Ions in Matter, Vol. 5, edited by J. F. Ziegler, (Pergamon, Oxford, 1980).
[36] U. Littmark and J. F. Ziegler, in *Handbook of Range Distributions for Energetic Ions in All Elements*, The Stopping and Ranges of Ions in Matter, Vol. 6, edited by J. F. Ziegler (Pergamon, Oxford, 1980).
[37] C. T. Chantler, J. Appl. Crystallogr. **25**, 674 (1992).
[38] C. T. Chantler, J. Appl. Crystallogr. **25**, 694 (1992).
[39] L. T. Hudson, R. D. Deslattes, A. Henins *et al.*, Med. Phys. **23**, 1659 (1996).
[40] C. T. Chantler, R. D. Deslattes, A. Henins, and L. T. Hudson, Br. J. Radiol. **69**, 636 (1996).
[41] C. T. Chantler and R. D. Deslattes, Rev. Sci. Instrum. **66**, 5123 (1995).
[42] B. L. Henke *et al.*, At. Data Nucl. Data Tables **27**, 1 (1982).
[43] K. Omidvar, At. Data Nucl. Data Tables **28**, 1 (1983).
[44] E. Takacs, E. S. Meyer, J. D. Gillaspy, *et al.*, Phys. Rev. A **54**, 1342 (1996).
[45] A. Chetioui *et al.*, J. Phys. B **16**, 3993 (1983).
[46] L. A. Vainshtein and U. I. Safranova, At. Data Nucl. Data Tables **21**, 49 (1978).
[47] J. M. Laming, Nucl. Instrum. Methods Phys. Res. B **43**, 359 (1989).

[48] L. A. Vainshtein and U. I. Safranova, At. Data Nucl. Data Tables **25**, 311 (1980).
[49] G. W. F.Drake, in *The Spectrum of Atomic Hydrogen: Advances*, edited by G. W. Series (World Scientific, Singapore, 1988), pp. 137–241.
[50] H. J. Hay and P. B. Treacy, Aust. J. Phys. **40**, 125 (1987).
[51] A. Corney, *Atomic and laser spectroscopy* (Clarendon, Oxford, 1986).
[52] E. U. Condon and G. H. Shortley, *The Theory of Atomic Spectra* (CUP, Cambridge, 1987).
[53] C. T. Chantler, J. Phys. Chem. Ref. Data **24**, 71 (1995).
[54] C. T. Chantler, J. Phys. Chem. Ref. Data **29**, 597 (2000).
[55] R. Anholt, Phys. Rev. A **31**, 3579 (1985).
[56] R. H. Pratt, Phys. Rev. **117**, 1017 (1960).
[57] W. E. Meyerhof, R. Anholt, J. Eichler, H. Gould, C. Munger, J. Alonso, P. Thieberger, and H. E. Wegner, Phys. Rev. A **32**, 3291 (1985).
[58] R. Anholt *et al.*, Phys. Rev. A **33**, 2270 (1986).
[59] L. J. Dubé and J. Eichler, J. Phys. B **18**, 2467 (1985).
[60] J. Eichler and F. T. Chan, Phys. Rev. A **20**, 104 (1979).
[61] J. S. Briggs and L. J. Dubé, J. Phys. B **13**, 771 (1980).
[62] L. J. Dubé, J. Phys. B **17**, 641 (1984).
[63] H. A. Bethe and E. E. Salpeter, *Quantum Mechanics of One- and Two-Electron Atoms* (Plenum, New York, 1977).
[64] R. Anholt and W. E. Meyerhof, Phys. Rev. A **33**, 1556 (1986).
[65] R. Anholt, W. E. Meyerhof, H. Gould, C. Munger, J. Alonso, P. Thieberger, and H. E. Wegner, Phys. Rev. A **32**, 3302 (1985).
[66] R. Anholt *et al.*, Phys. Rev. A **30**, 2234 (1984).
[67] J. H. Hubbell *et al.*, J. Phys. Chem. Ref. Data **4**, 471 (1975).
[68] G. S. Khandelwal *et al.*, At. Data **1**, 103 (1969).
[69] B.-H. Choi *et al.*, At. Data **5**, 291 (1973).
[70] J. M. Hansteen *et al.*, At. Data Nucl. Data Tables **15**, 305 (1975).
[71] M. R. C. McDowell and J. P. Coleman, *Introduction to the Theory of Ion-Atom Collisions* (North-Holland, London, 1970).
[72] J. P. Rozet *et al.*, Phys. Rev. Lett. **58**, 337 (1987).
[73] J. P. Rozet and A. Chetioui, J. Phys. B **14**, 73 (1981).
[74] H. F. Beyer, K. D. Finlayson, D. Liesen *et al.*, J. Phys. B **26** 1557 (1993).
[75] C. T. Chantler, Radiat. Phys. Chem. **41**, 759 (1993).
[76] C. T. Chantler, in *Resonant Anomalous X-Ray Scattering: Theory and Applications*, edited by G. Materlik, K. Fischer, and C. J. Sparks, (Elsevier, North-Holland, 1994), pp. 61–78.
[77] W. A. Hallett, Ph.D. Thesis, Oxford University, 1991.
[78] S. MacLaren, P. Beiersdorfer, D. A. Vogel, D. Knapp, R. E. Marrs, K. Wong, and R. Zasadzinski, Phys. Rev. A **45** 329 (1992).
[79] D. R. Plante, W. R. Johnson, and J. Sapirstein, Phys. Rev. A **49**, 3519 (1994).
[80] M. H. Chen, K. T. Cheng, and W. R. Johnson, Phys. Rev. A **47**, 3692 (1993); K. T. Cheng, M. H. Chen, W. R. Johnson, and J. Sapirstein, *ibid.* **50**, 247 (1994).
[81] P. Indelicato, Nucl. Instrum. Methods Phys. Res. B **31**, 14 (1988); P. Indelicato, O. Gorceix, and J. P. Desclaux, J. Phys. B **20**, 651 (1987); P. Indelicato, F. Parente, and R. Marrus, Phys. Rev. A **40**, 3505 (1989).
[82] K. T. Cheng and M. H. Chen, Phys. Rev. A **61**, 044503 (2000).
[83] R. D. Deslattes, H. F. Beyer, and F. Folkmann, J. Phys. B **17**, L689 (1984).
[84] J.-P. Briand, J. P. Mosse, P. Indelicato, P. Chevallier, D. Girard-Vernhet, A. Chetioui, M. T. Ramos, and J. P. Desclaux, Phys. Rev. A **28**, 1413 (1983).
[85] M. R. Tarbutt, R. Barnsley, N. J. Peacock, and J. D. Silver, J. Phys. B **34**, 3979 (2001).
[86] P. Richard, M. Stockli, R. D. Deslattes, P. Cowan, R. E. LaVilla, B. Johnson, K. Jones, M. Meron, R. Mann, and K. Schartner, Phys. Rev. A **29**, 2939 (1984).
[87] E. Källne, J. Källne, P. Richard, and M. Stöckli, J. Phys. B **17**, L115 (1984).
[88] R. D. Deslattes, R. Schuch, and E. Justiniano, Phys. Rev. A **32**, 1911 (1985).
[89] H. F. Beyer, R. D. Deslattes, F. Folkmann, and R. E. La Villa, J. Phys. B **18**, 207 (1985).
[90] E. S. Marmar, J. E. Rice, E. Källne, J. Källne, and R. E. LaVilla, Phys. Rev. A **33**, 774 (1986).
[91] H. D. Dohmann, D. Liesen, and E. Pfeng, Proceeding of the Eighth ICPEAC, Berlin, 1983 (unpublished), p. 467; GSI Scientific Report No. 1982, 1983 (unpublished), p. 155.
[92] M. R. Tarbutt and J. D. Silver, J. Phys. B **35**, 1467 (2002).
[93] J.-P. Briand, M. Tavernier, P. Indelicato, R. Marrus, and H. Gould, Phys. Rev. Lett. **50**, 832 (1983).
[94] A. F. McClelland, Ph.D. Thesis, Oxford University, (1989).
[95] H. F. Beyer, R. D. Deslattes, P. Indelicato, K. D. Finlayson, and D. Liesen, GSI Annual Report, (1989) (unpublished), p. 143.
[96] J.-P. Briand, M. Tavernier, R. Marrus, and J. P. Desclaux, Phys. Rev. A **29**, 3143 (1984).
[97] C. T. Chantler and J. A. Kimpton, Can. J. Phys. (to be published).
[98] L. Schleinkofer, F. Bell, H.-D. Betz, G. Trollmann, and J. Rothermel, Phys. Scr. **25**, 917 (1982).
[99] H. Gould and C. T. Munger, *Atomic Physics*, edited by H. Narumi and I. Shimamura (Elsevier, Amsterdam, 1987), Vol. 10, pp. 77–93.
[100] J. P. Buchet, M. C. Buchet-Poulizac, A. Denis, J. Desesquelles, M. Druetta, J. P. Grandin, and X. Husson, Phys. Rev. A **23**, 3354 (1981).
[101] R. DeSerio, H. G. Berry, R. L. Brooks, J. Hardis, A. E. Livingston, and S. J. Hinterlong, Phys. Rev. A **24**, 1872 (1981).
[102] T. J. Scholl, R. A. Holt, and S. D. Rosner, Phys. Rev. A **39**, 1163 (1989).
[103] P. Zhao, J. R. Lawall, A. W. Kam, M. D. Lindsay, F. M. Pipkin, and W. Lichten, Phys. Rev. Lett. **63**, 1593 (1989).
[104] M. N. Kinnane, J. A. Kimpton, M. D. de Jonge, K. Makonyi, and C. T. Chantler, Meas. Sci. Technol. **16**, 2280 (2005).
[105] J. A. Kimpton, M. N. Kinnane, and C. T. Chantler, Rev. Sci. Instrum. **77**, 083102 (2006).
[106] C. T. Chantler, D. Paterson, L. T. Hudson, F. G. Serpa, J. D. Gillaspy, and E. Takacs, Phys. Scr., T **80B**, 440 (1999).
[107] C. T.Chantler, M. N. Kinnane, C.-H. Su, and J. A. Kimpton, Phys. Rev. A **73**, 012508 (2006).
[108] M. N. Kinnane, J. A. Kimpton, and C. T. Chantler, Radiat. Phys. Chem. **75**, 1744 (2006).
[109] C. T. Chantler, Radiat. Phys. Chem. **71**, 611 (2004).
[110] E. G. Myers, Ph.D. thesis, Oxford University (1981).
[111] E. G. Myers, Nucl. Instrum. Methods Phys. Res. B **9**, 662 (1985).
[112] E. G. Myers, P. Kuske, H. J. Andrä, I. A. Armour, N. A. Jelley, H. A. Klein, J. D. Silver, and E. Träbert, Phys. Rev.

Lett. **47**, 87 (1981).
[113] E. G. Myers, J. K. Thompson, H. S. Margolis, J. D. Silver, and M. R. Tarbutt, Hyperfine Interact. **127**, 323 (2000).
[114] H. J. Andrä, Nucl. Instrum. Methods Phys. Res. **202**, 123 (1982).
[115] K. Hosaka, D. N. Crosby, K. Gaarde-Widdowson, C. J. Smith, J. D. Silver, T. Kinugawa, S. Ohtani, and E. G. Myers, Phys. Rev. A **69**, 011802 (2004).
[116] H. Gould and R. Marrus, Phys. Rev. A **28**, 2001 (1983).
[117] A. P. Georgiadis, *et al.*, Phys. Lett. A **115**, 108 (1986).
[118] G. W. F. Drake, J. Patel, and A. van Wijngaarden, Phys. Rev. Lett. **60**, 1002 (1988).